A Dynamic and Thermodynamic Foundation for Modeling the Moist Atmosphere with Parameterized Microphysics

KATSUYUKI V. OOYAMA

Hurricane Research Division, AOML, NOAA, Miami, Florida

(Manuscript received 14 March 2000, in final form 2 November 2000)

ABSTRACT

Moist convection is an exquisite yet powerful participant in the creation of weather on our planet. To facilitate numerical modeling of weather systems in a moist atmosphere, a direct and consistent application of dynamic and thermodynamic principles, in conjunction with parameterized microphysics, is proposed. An earlier formulation of reversible thermodynamics, in terms of the mass of air and water substance and the total entropy, is now extended to include the irreversible process of precipitation through parameterized microphysics. The dynamic equations are also formulated to account consistently for the mass and momentum of precipitation.

The theoretical proposal is tested with a two-dimensional model that utilizes a versatile and accurate spectral method based on a cubic-spline representation of the spatial fields. In order to allow a wide range of scale interactions, the model is configured on multiply nested domains of outwardly decreasing resolution, with noise-free, two-way interfaces. The semi-implicit method provides efficient time integration for the nested spectral model.

The tests performed are the simulation of the growth of single-cell clouds and also the generation of self-sustaining multicell squall lines, and the effects of various resolutions on the simulations are examined. The results favorably compare with similar results found in the literature, but also offer new insights into the interplay between dynamics and precipitation.

1. Introduction

In the Tropics, moist convection dominates the process of transporting mass, energy, and momentum through the atmosphere. At the heart of the process are short-lived, cloud-scale cells driven by latent heat from condensing water vapor. The dynamics of individual cells are in a stochastic regime of turbulence (Ooyama 1982), and the extra mode of transport by precipitation of condensed water adds to their complexity. General confinement of convection by the ground and the stable stratosphere forces neighboring cells to interact, promoting mesoscale organization of cells. On longer timescales, the large-scale environment can influence and control the mesoscale organization and activities. Our problem, here, is how to handle this long chain of multiscale interactions in numerical models of weather systems. The genesis of tropical cyclones is a particular example that has motivated the present study.

In those models that do not resolve cloud scales, moist convection is usually parameterized. While this is a reasonable approach under such limitations, parameterization has remained largely a heuristic art, due to the lack of a clear spectral gap between explicit field variables and implicit clouds, which a more deductive theory could have exploited. To overcome this ambiguity, a number of cloud-resolving models have been developed, starting from early works by Ogura and Takahashi (1971), Yamasaki (1977), Klemp and Wilhelmson (1978), etc., and culminating in institutionally developed general-purpose models, such as MM5 (http://www.mmm.ucar.edu/mm5/doc.html) and ARPS (http://wwwcaps.ou.edu:80/ARPS/). Applying these models, it is now possible to study a variety of mesoscale phenomena with explicit convection.

The model proposed in this paper is not ready for general application. At present, it is spatially two-dimensional in x and z on a flat earth (no terrain); the microphysics of precipitation is parameterized by a Kessler-type formulation; no radiative transfer is included; and only a crude formulation of eddy fluxes in the atmospheric boundary layer, above the constant-flux surface layer, has been attempted. What is offered, instead, is a formulation of dynamic and thermodynamic principles and a clean strategy of nested spectral modeling, both of which can later be extended to more comprehensive models. It is believed, however, that the model in its present form can be utilized for understanding both the enormous complexity of moist convection and the role of many critical options that have to be chosen in numerical simulations of particular events.

Corresponding author address: Katsuyuki V. Ooyama, Hurricane Research Division, AOML, NOAA, 4301 Rickenbacker Causeway, Miami, FL 33149.
E-mail: yy@aoml.noaa.gov

It was proposed in Ooyama (1990), referred hereafter as O90, that the separation of dynamics and thermodynamics by their primary roles would simplify the theoretical design of numerical models of the moist atmosphere. The role of dynamics is to predict temporal changes in the spatial distribution of conservative properties, such as mass, momentum, and entropy (or internal energy), while that of thermodynamics is to diagnose relevant states of each chemical component of matter, such as pressure, temperature, and phases of water. A few assumptions were made in O90: water vapor was treated as an ideal gas, the volume of condensed water was neglected, and the ice phase was continuously merged with the liquid phase into a synthesized, single phase of condensate. Otherwise, the theory closely followed the classical formulation of reversible thermodynamics.

In order to allow precipitation in the model, however, the thermodynamics must be generalized to include irreversible microphysical processes. This can be achieved, as shown in section 2, by a simple extension of the reversible theory of O90, provided that the irreversible processes are parameterized. Comments on other irreversible processes are given in appendix B. As for the dynamics, we had earlier thought that the prognostic equations based on conservation principles were well established, until a problem was discovered in the equation of vertical momentum when parameterized precipitation was included. A consistent resolution of the problem is discussed in section 3. Computational adaptation of those equations, including a remedy for the computational *negative* water, is given in section 4.

The finiteness of computational resources constrains the design of numerical models. In a cloud-resolving model of weather systems, the required range of spacial scales may possibly run from 0.1 to 1000 km. We have decided to adopt the strategy of domain nesting to allow such a range of scales in a single model, although it presumes that the convective activities of interest are confined to the inner domains of finer resolution. We have also decided on a spectral representation of the spatial fields by cubic splines, because accuracy in computational phase speeds is essential to noise-free, two-way nesting. The essence of this numerical method has been described in DeMaria et al. (1992) and is summarized in section 5.

Two series of experiments with the model are demonstrated in this paper. Simulation of a single cloud cell in various spatial resolutions is discussed in section 6, and the generation of a squall line in a sheared environment in section 7. A benchmark test of the model is also given in appendix C. The results favorably compare with those of similar studies in the literature. Problems for future work are discussed in the final section.

2. Thermodynamic diagnosis

a. Mass variables

The atmosphere we consider is made of dry air and water substance. The water substance is recognized in two phases, vapor and condensate (liquid or solid). The condensate is further classified in two modes, airborne and precipitating. The distinction occurs from the difference in implied particle size. Due to its small particle size, airborne condensate (cloud) is in instantaneous equilibrium and moves together with the environment of moist air in which it is suspended. Due to its greater drop size and smaller surface-to-volume ratio, the precipitating condensate (rain or snow) needs time to adjust itself to the environment through which it falls. Thus, the spatial distribution of precipitating water must be predicted separately from that of airborne moisture (the sum of vapor and airborne condensate), with due consideration of the conversion between phases and between modes.

The estimation of those conversion rates is greatly facilitated by the adoption of a Kessler-type parameterization of the microphysics. The boldest assumption by Kessler (1969) is to collapse the drop size–dependent processes into a set of a few formulas written in terms of the precipitation water content (a single scalar), by integrating them over an assumed drop size distribution. The specific formulas, adopted from Klemp and Wilhelmson (1978), are listed in appendix A.

Ideally, the liquid and ice phases of the condensate should be separate. In active clouds, however, the two phases are hardly in equilibrium; and, moreover, the ice has various crystal forms and various degrees of aggregation. In order to avoid the complication of a nonequilibrium mixture, O90 synthesized a single, continuous phase of condensate that would behave, with respect to vapor, like liquid or ice, depending on temperature. The synthesis was made by smoothing the Kirchhoff equation across a freezing zone of temperature, in such a way that all three phases of water were consistently modified. The smoothed saturation vapor pressure was practically unchanged from the original, either over liquid or over ice depending on temperature, but the latent heat of fusion was replaced by a large anomaly of the specific heat of the synthesized condensate in the freezing zone. This approximation is adopted in the present model. Accordingly, we do not introduce additional formulas for parameterizing ice–form interactions, except for reducing the fall speed of our single-phase precipitation when the temperature is below the freezing point.

The mass variables are expressed as densities in geometrical space. Since the symbols used in O90 for this purpose have proved to be rather unpopular, we revert here to the more traditional density symbol, ρ, with subscripts. Namely, ρ_a stands for dry air, ρ_v for vapor, ρ_c for airborne condensate (cloud), and ρ_r for precipitating condensate (‘‘rain’’ and ‘‘snow’’ in our extended sense). We also define $\rho_m = \rho_v + \rho_c$ for the total airborne moisture, and $\rho = \rho_a + \rho_m + \rho_r$ for the total mass per unit volume. As discussed below, ρ_v and ρ_c are not independently predicted, but diagnostically separated from the predicted ρ_m.

b. Entropy

The first law of thermodynamics concerns energy conservation and can be expressed in terms of the internal energy, entropy, or enthalpy. In a model of the moist atmosphere on the geometrical coordinates, the entropy, in our view, is the most convenient variable to express the conservation law. In the meteorology of the dry atmosphere, the potential temperature is the prevalent variable employed for the same purpose, but it is merely an exponential transform of the entropy expressed in units of temperature. The equivalent potential temperature is also widely used in studies of the moist atmosphere, although it is only approximately conservative due to the assumption of the pseudoadiabatic process. Various proposals, such as Betts (1973) and Tripoli and Cotton (1981), have been made to define a potential temperature that more rigorously handles the phase changes of water substance. Hauf and Höller (1987) have argued that those definitions are covered by the entropy temperature, which they defined directly from the entropy. In the present paper, the entropy itself is used as one of the prognostic variables. If so desired, a conversion of the entropy to an equivalent variable in temperature units can be easily made from the model output.

If all the processes are adiabatic and reversible, the entropy is strictly conserved. This is assumed to be the case with respect to phase transitions of water substance within the moist atmosphere. On the other hand, certain important processes in the real atmosphere, such as the diffusive mixing or the generation of precipitation, are irreversible. The common practice in modeling is to add the effects of those irreversible processes to the conservation equations in the form of parameterized sources and sinks. In this regard, the present model shares the same basic premise with other dynamic models of the atmosphere. Nevertheless, it will be prudent to ascertain that the employed parameterization does not violate the second law of thermodynamics. Further discussions on the second law are given in appendix B.

One unique feature in the formulation of the present model is our treatment of the pressure. The prevailing practice in atmospheric modeling is to predict the pressure by a tendency equation which is derived from the combination of dynamic and thermodynamic principles. Although the derivation for the dry atmosphere is straightforward, the corresponding one for the moist atmosphere becomes entangled with the complexity of moist thermodynamics. According to the classical dictum of thermodynamics, the pressure is a state variable that, along with the temperature, can be diagnostically determined from the mass and entropy. Thus, it was proposed by O90 to separate the dynamics out of the determination of the pressure. Even in hydrostatic models, as discussed by O90 and demonstrated by DeMaria (1995), this approach eliminates Richardson's problem of an awkward ''*w* equation'' on the height-coordinate. In nonhydrostatic moist models, the same approach also allows a stylistically simple yet accurate set of prognostic equations and facilitates the logistics of solution.

The entropy per unit volume may be defined for each mass component in the volume, that is, σ_a for the dry air, σ_m for the airborne moisture (vapor and cloud), and σ_r for the precipitating water. In the present model, however, only the total entropy density, $\sigma = \sigma_a + \sigma_m + \sigma_r$, needs to be predicted. In particular, as explained below, it does not require a separate prediction of σ_r.

c. Temperature

In the absence of precipitation, O90 defined two equilibrium states of moist air that were possible for a set of predicted values of ρ_a, ρ_m, and σ. State 1, at temperature T_1, is characterized by the absence of condensate, even if the vapor is supersaturated. State 2 is characterized by the vapor being saturated at temperature T_2, even by evaporating borrowed water if necessary. The two temperatures are diagnostically determined by solving, respectively,

$$\sigma = S_1(\rho_a, \rho_m, T_1) \quad \text{and} \quad \sigma = S_2(\rho_a, \rho_m, T_2)$$

for known thermodynamic functions S_1 and S_2 (see appendix B). For reasons discussed in O90, the realistic temperature T, without supersaturation or borrowed water, should be the greater of T_1 and T_2, while T_2 is always identifiable as the wet-bulb temperature.

In the presence of precipitation, the procedure requires a few modifications. Since all the matter in state 2 is at the same wet-bulb temperature, T_2 can be determined first, by solving

$$\sigma = S_2(\rho_a, \rho_m + \rho_r, T_2), \tag{2.1}$$

where the predicted σ now contains σ_r. It is noted that, if water must be ''borrowed'' to saturate the air, it should not come from ρ_r but from ρ_c. Any change in ρ_r should occur during prediction in time, not in the diagnostic procedure at a fixed time, while ρ_c is mathematically allowed to become negative in diagnostic calculations.

In determining state 1, the role of precipitation is equally passive; although ρ_c is constrained to zero, ρ_r remains unchanged. Since T_2 has been determined by (2.1), σ_r is already known by

$$\sigma_r = \rho_r C(T_2), \tag{2.2}$$

where $C(T_2)$ is the specific entropy of condensate at T_2. Thus, all the effects of precipitation can be discounted in the equilibrium equation for state 1, and T_1 is obtained by solving

$$\sigma - \sigma_r = S_1(\rho_a, \rho_m, T_1). \tag{2.3}$$

The realizable temperature T is determined by

$$T = \max(T_1, T_2). \tag{2.4}$$

It is noted that (2.2) is based on an idealization that the temperature of raindrops is at the wet-bulb temperature in unsaturated air. Kinzer and Gunn (1951) observed the relaxation time of raindrop temperature to be approximately 4.35 s. This rapid relaxation is due to the small amount of heat required to adjust the temperature of a raindrop as compared to that required to evaporate it. Thus, in unsaturated air, ρ_r must be predicted with a parameterized evaporation rate, but σ_r is a known quantity once the wet-bulb temperature is diagnosed. The exchange of both the sensible and latent heat between the raindrops and gaseous environment is internal to the prediction of the total entropy. In saturated conditions, the temperature itself is the wet-bulb temperature, and there is thermodynamically no difference between cloud and precipitation.

d. Pressure and other state variables

Once the temperature is known, the total pressure, p, is given by

$$p = p_a + p_v, \tag{2.5}$$

where the partial pressures, p_a for dry air and p_v for vapor, are determined by

$$p_a = \rho_a R_a T, \qquad p_v = \begin{cases} \rho_m R_v T & \text{if } T = T_1, \\ E(T) & \text{if } T = T_2, \end{cases} \tag{2.6}$$

where $E(T)$ is the saturation vapor pressure. The vapor density and cloud water content are

$$\rho_v = (R_v T)^{-1} p_v, \qquad \rho_c = \rho_m - \rho_v. \tag{2.7}$$

Note that, if $T = T_1$, $\rho_m = \rho_v$ and $\rho_c = 0$.

3. Prognostic equations in flux form

a. Definitions and clarifications

Our working model is two-dimensional in the vertical plane and can be run in either of two modes: slab symmetric or axisymmetric. Since the model will eventually be three-dimensional, the dynamic equations below are given in 3D on an f plane, written in Cartesian coordinates (x, y, z). We use vector notation for the horizontal (x, y) components, and the vertical component will be written separately. This is because the fall speed of precipitation W is purely vertical, and its place in the vertical momentum equation needs to be highlighted. Thus, $(\mathbf{v}, w)$ denotes the velocity of both dry air and airborne moisture (vapor and cloud), while $(\mathbf{v}, w_r)$ denotes the velocity of precipitating water, with $w_r = w + W$. The sign convention for w and W are the same, so that W is always negative (downward).

When ρ_c (cloud) is present in saturated air, it may be converted to ρ_r (precipitation), by autoconversion and collection processes, at a finite rate Q_r. When ρ_r is present in unsaturated air, it evaporates back to ρ_v (vapor) at a finite rate, which will be denoted by a negative value of Q_r. Since both ρ_v and ρ_c are part of the total airborne water ρ_m, we may treat Q_r, either positive or negative, as the conversion rate between ρ_m and ρ_r. Parametric formulas for Q_r and W are given in the appendix A.

Other physical processes, such as radiative heat transfer, boundary layer eddy fluxes, and internal diffusive processes, are not included in the present discussion. A Newtonian cooling may be added to the entropy prediction, but a more realistic formulation of radiative fluxes is outside the scope of this paper. Model experiments that run more than a few hours should include interactions of the atmosphere with the underlying surface. Although a conventional formulation of the constant-flux surface layer and a crude formulation of eddy fluxes in the mixed layer are included in our model, these are not utilized in the experiments reported in this paper.

The omission of internal diffusion terms from our equations is deliberate and requires a clarification. In general, models of finite resolution must avoid the accumulation of spectral power near the Nyquist wavelength ($2\Delta x$). Such a problem may occur due to either the inherent spectral cascades in nonlinear dynamics or the numerical accuracy in handling the smallest scales. Although these causes are often inseparable, the problem is usually abated by the inclusion of diffusion terms, attributed to ‘‘subgrid-scale’’ turbulence. In the present model, a low-pass filter that is built into the spectral transform (see section 5b) is applied to every prognostic variable at each time step. Although the filter is designed primarily for reducing the spectral representation error in 2 to $3\Delta x$ waves, it also effectively eliminates the spectral accumulation in these scales that is due to nonlinear cascades. Thus, additional diffusion terms are found unnecessary for computational stability and are omitted in our equations. On the other hand, since the built-in filter has a sharp cutoff taper of the sixth order, the filter will not override the added effects of the second- or fourth-order diffusion, if such effects are called for by the model physics. (See appendix C for a demonstration.)

b. Conservation equations for mass and entropy

The continuity equations for the mass variables, ρ_a, ρ_m, and ρ_r, are given by

$$\partial_t \rho_a + \nabla \cdot (\rho_a \mathbf{v}) + \partial_z(\rho_a w) = 0, \tag{3.1}$$

$$\partial_t \rho_m + \nabla \cdot (\rho_m \mathbf{v}) + \partial_z(\rho_m w) = -Q_r, \tag{3.2}$$

$$\partial_t \rho_r + \nabla \cdot (\rho_r \mathbf{v}) + \partial_z(\rho_r w_r) = Q_r. \tag{3.3}$$

These three equations are independent and may be combined into other convenient forms. In particular, the sum of the three gives the equation for the total mass,

$$\partial_t \rho + \nabla \cdot (\rho \mathbf{v}) + \partial_z(\rho w + \rho_r W) = 0. \tag{3.4}$$

Obviously, there is no internal source of mass; but, since W does not vanish at the ground, the second term of the vertical mass flux implies a loss of precipitating water to the ground.

Similarly, the equation for the total entropy is given by

$$\partial_t \sigma + \nabla \cdot (\sigma \mathbf{v}) + \partial_z(\sigma w + \sigma_r W) = 0. \quad (3.5)$$

Internal heat exchanges among various constituents are balanced out, although there is, again, a loss of entropy to the ground due to precipitation.

c. Conservation equations for momentum

The horizontal momentum equation for the total mass, including precipitation, is

$$\partial_t(\rho \mathbf{v}) + \nabla \cdot (\rho \mathbf{v}\mathbf{v}) + \partial_z[(\rho w + \rho_r W)\mathbf{v}] + f\mathbf{k} \times (\rho \mathbf{v}) + \nabla p = 0, \quad (3.6)$$

where, in the third term, $\rho_r W$ supplements ρw to account for the vertical flux of horizontal momentum by precipitation.

Since the pressure gradient force acts on volume, it does not directly accelerate the condensate whose volume is negligibly small. Nevertheless, even in accelerating conditions, no relative horizontal motion is assumed between the condensate and gaseous environment. This implies that a frictional drag force instantaneously eliminates any velocity difference. For the total mass, the action and reaction balance out internally.

The circumstance is a little different in the vertical. To illustrate the problem, we write the vertical momentum equations separately for $\rho_{am} = \rho_a + \rho_m$ and ρ_r. The vertical component of velocity is w for the former, and $w_r = w + W$ for the latter. Specifically,

$$\partial_t(\rho_{am} w) + \nabla \cdot (\rho_{am} w \mathbf{v}) + \partial_z(\rho_{am} w w) + \rho_{am} g + \partial_z p = -F_r - Q_r w, \quad \text{and} \quad (3.7)$$

$$\partial_t(\rho_r w_r) + \nabla \cdot (\rho_r w_r \mathbf{v}) + \partial_z(\rho_r w_r w_r) + \rho_r g = F_r + Q_r w_r, \quad (3.8)$$

where F_r is the vertical component of frictional drag force acting on ρ_r, and its reaction on ρ_{am}. The pressure gradient force on ρ_r is, again, negligible.

The sum of (3.7) and (3.8) yields an equation for the total vertical momentum:

$$\partial_t(\rho w + \rho_r W) + \nabla \cdot \{(\rho w + \rho_r W)\mathbf{v}\} + \partial_z\{\rho w w + \rho_r W(2w + W)\} + \rho g + \partial_z p = Q_r W, \quad (3.9)$$

in which F_r is balanced out, but a source term, $Q_r W$, remains as the residual of $-Q_r w$ and $Q_r w_r$.

To explain the cause of this residual source, let us assume for the moment that Q_r is positive. Then, the term $-Q_r w$ on the rhs of (3.7) represents a rate of momentum loss in ρ_{am} simply due to the fact that part of ρ_m moving with velocity w is reclassified to be part of ρ_r. The same reclassified mass appears in (3.8) as a momentum source but with velocity w_r. This sudden acceleration is due to the gravity acting on raindrops (or snow) before it becomes fully opposed by F_r. Therefore, the source term is legitimate, except for the idealization that the acceleration takes place instantaneously as soon as the parameterization reclassifies airborne condensate to precipitation. If Q_r is negative, it is an instantaneous deceleration that accompanies the reclassification of precipitation to vapor.

As a prognostic equation, however, (3.9) has a logical contradiction. The contradiction is actually inherited from (3.8), which considers w_r to be a prognostic variable. Since w itself is predictable by (3.7), these equations are in fact predicting W, in spite of our assumption to parameterize. In terms of prognostic calculations, (3.9) also presents practical difficulties to a numerical scheme which requires a priori specification of the lower boundary condition on $(\rho w + \rho_r W)$. An attempt to ignore only the local time derivative of W leaves physically unacceptable source/sink terms in the kinetic energy budget. Theoretically, we can choose to predict W, by removing it from the list of parameterized variables. This option, however, may lead to the total abandonment of the microphysics parameterization, because W is intimately involved in the estimation of F_r and Q_r. In order to stay the course, (3.8) and (3.9) must be somehow modified to be compatible with the diagnostic determination of W.

This dilemma has a well-known precedent in the quasistatic system of equations. The customary resolution is to ignore the material derivative of w in the equation of vertical motion, while w is diagnostically derived from the hydrostatic equation (e.g., O90), although this leads to a counterintuitive consequence that the kinetic energy budget will not contain the contribution of the vertical motion. As observed by Eliassen and Kleinschmidt (1957, 20–21), this is commonly accepted as a *plausible* approximation without rigorous justification.

In the present nonhydrostatic case in which w is fully prognostic, an analogous principle may be applied to the terminal fall speed W. Namely, we postulate that the material derivative of W along the path of precipitation,

$$D_t^{(r)} W \equiv \partial_t W + \mathbf{v} \cdot \nabla W + w_r \partial_z W, \quad (3.10)$$

be ignored in (3.8), which then is reduced to

$$\partial_t(\rho_r w) + \nabla \cdot (\rho_r w \mathbf{v}) + \partial_z(\rho_r w w_r) + \rho_r g - F_r = Q_r w. \quad (3.11)$$

Similarly, (3.9) for the total vertical momentum is replaced by

$$\partial_t(\rho w) + \nabla \cdot (\rho w \mathbf{v}) + \partial_z[(\rho w + \rho_r W)w] + \rho g + \partial_z p = 0, \quad (3.12)$$

which is the sum of (3.11) and (3.7).

Although the kinetic energy equation is not used in prediction, it is interesting to see how it comes out of the new set of prognostic equations. From (3.6) and (3.12) with the aid of (3.1)–(3.4), an equation for the total mechanical energy is derived as

$$\partial_t(K + \Phi) + \boldsymbol{\nabla} \cdot [(K + \Phi + p)\mathbf{v}] + \partial_z[(K + \Phi + p)w + (K_r + \Phi_r)W] = p(\boldsymbol{\nabla} \cdot \mathbf{v} + \partial_z w) + g\rho_r W, \tag{3.13}$$

with the definitions

$$K \equiv \rho(\mathbf{v}^2 + w^2)/2, \qquad \Phi \equiv g\rho z,$$
$$K_r \equiv \rho_r(\mathbf{v}^2 + w^2)/2, \qquad \Phi_r \equiv g\rho_r z, \tag{3.14}$$

where K and Φ are the total kinetic and potential energy per unit volume, respectively; and K_r and Φ_r of the precipitation alone are defined for the convenience of notation, although these are part of the total. As expected, the kinetic energy does not contain any contribution from W in this energy budget of the modified system.

On the rhs of (3.13), the first term is the mechanical work done by the changing specific volume against pressure and constitutes the link with the internal energy of gaseous matter. The second term is always negative, as W is, and represents the dissipation of kinetic energy of precipitation due to work done by the frictional drag against falling precipitation (i.e., F_rW), although F_r is replaced by the nearly equivalent $g\rho_r$ under the present approximation. In the third term on the lhs of (3.13), the extra flux by W does not vanish at the ground and represents a loss of the mechanical energy from the atmosphere; K_r will be lost on impact, though, on elevated terrain, Φ_r is still retained by the ground water so that it can run downhill.

In conclusion, we shall accept (3.12) as a *plausible* and consistent approximation for the vertical momentum equation. In more practical terms, numerical discrepancies that may arise from ignoring (3.10) are expected to be slight, because W varies rather slowly with a small fractional power of ρ_r and the square root of ρ_a, with possible minor exceptions in the melting zone.

4. Computational adaptation

a. The equations in advective form

For the convenience of numerical calculations, the equations in the preceding section are converted to equivalent equations in advective form. Since our numerical method utilizes differentiable spectral bases, the conversion does not alter the conservativeness of the original flux form.

The water mass variables are normalized by dry air; that is, the mixing ratios[1] are defined as $\mu_m = \rho_m/\rho_a$, $\mu_r = \rho_r/\rho_a$, and $\mu = \mu_m + \mu_r$. Similarly, we define the dry-air specific entropy $s = \sigma/\rho_a$. The advection operator is abbreviated as

$$D_t(\,) \equiv \partial_t(\,) + \mathbf{v} \cdot \boldsymbol{\nabla}(\,) + w\partial_z(\,). \tag{4.1}$$

For the mass equations, (3.1) through (3.4) are now written as

$$D_t(\ln\rho_a) + (\boldsymbol{\nabla} \cdot \mathbf{v} + \partial_z w) = 0, \tag{4.2}$$
$$D_t\mu_m = -\rho_a^{-1}Q_r, \tag{4.3}$$
$$D_t\mu_r = \rho_a^{-1}[Q_r - \partial_z(\rho_r W)], \tag{4.4}$$
$$D_t\mu = -\rho_a^{-1}\partial_z(\rho_r W). \tag{4.5}$$

Of the last three equations for water substance, only two are independent and actually used in prediction. Our preference is (4.4) and (4.5).

For the entropy, (3.5) becomes

$$D_t s = -\rho_a^{-1}\partial_z(\sigma_r W). \tag{4.6}$$

For the horizontal and vertical components of velocity, (3.6) and (3.12) respectively yield

$$D_t\mathbf{v} + f\mathbf{k} \times \mathbf{v} + \rho^{-1}\boldsymbol{\nabla} p = -\rho^{-1}\rho_r W\partial_z\mathbf{v}, \tag{4.7}$$
$$D_t w + g + \rho^{-1}\partial_z p = -\rho^{-1}\rho_r W\partial_z w. \tag{4.8}$$

b. Background and deviations

The mass and thermodynamic states are strongly stratified in the atmosphere. By predicting deviations from predefined background states, rather than the full values of variables, we may gain a few decimal places in numerical accuracy. Such a gain is not trivial, since the model repeats prognostic calculations in small time steps a great number of times.

In general, the background may vary in space. At the present, it is defined to vary only in the vertical and will be indicated by a circumflex on appropriate symbols. For example, $\hat{\rho}_a$, $\hat{\rho}_m$, $\hat{\sigma}$, $\hat{p}$, etc. are functions of z defining the background states of respective variables. No background is assumed for precipitation, so that $\hat{\rho}_r = 0$ and $\hat{\rho} = \hat{\rho}_a + \hat{\rho}_m$.

We require that the background be a steady-state solution of the model. In particular, it must be in hydrostatic balance:

$$g\hat{\rho} + \partial_z\hat{p} = 0. \tag{4.9}$$

If the background is in motion, it should be in geostrophic or similar balance. Thus, the background states of model variables, such as density and entropy, can be diagnostically determined from readily observable variables, such as pressure, temperature, and relative humidity.

Although any part of the definitions for the background states may also be used for defining the initial states of a particular model run, the two states are conceptually independent; an individual run can be started

[1] In recent literature, the symbol for the mixing ratio varies between r and q. Historically (Huschke 1959), it was w, while q was for the specific humidity. We take the liberty of adopting μ for the mixing ratio as in O90.

from any set of initial states as long as it is physically possible.

The prognostic equations (4.2)–(4.8) are rewritten in terms of deviations, indicated by a prime. Since the transformation is rather mechanical, only a few examples are listed below.

With a shorthand notation, a, for the log-density of dry air (normalized by a constant reference density ρ_0),

$$a = \ln(\rho_a/\rho_0), \qquad \hat{a} = \ln(\hat{\rho}_a/\rho_0),$$
$$a' = a - \hat{a} = \ln(\rho_a/\hat{\rho}_a), \tag{4.10}$$

the mass continuity (4.2) becomes

$$D_t a' + w\partial_z \hat{a} + (\nabla \cdot \mathbf{v} + \partial_z w) = 0, \tag{4.11}$$

and, for the total water substance, (4.5) becomes

$$D_t \mu' + w\partial_z \hat{\mu} = -\rho_a^{-1}\partial_z(\rho_r W), \tag{4.12}$$

where, since $\hat{\mu}_r = 0$,

$$\hat{\mu} = \hat{\mu}_m, \qquad \mu' = \mu - \hat{\mu} = \mu'_m + \mu_r. \tag{4.13}$$

Another example of using deviations is given below.

c. Pressure gradient

From the predicted entropy and mass variables, the pressure at any spatial point can be determined by the diagnostic procedures of section 2. However, it is not the pressure itself but its spatial gradient that is required by (4.7) and (4.8). Since advective terms in those equations are calculated by the spectral transform method, it is not advisable to employ a finite-difference method to evaluate the pressure gradient. It was proposed in O90 to calculate the gradient with the aid of analytic differentiation of pressure in the manifold of thermodynamic variables. This method, derived for reversible thermodynamics, does not work well in the present case which includes irreversible processes of precipitation.

Therefore, although the pressure is a diagnostic variable, it has been decided to differentiate it by the spectral transform method, in the same way as the prognostic variables. For the sake of convenience, we define an auxiliary variable τ by

$$\tau = p/\rho_a, \tag{4.14}$$

which computationally takes the place of pressure. Since τ is approximately proportional to the temperature, its numerical range of variations is much smaller than that of the pressure. The background and deviations are also defined by

$$\hat{\tau} = \hat{p}/\hat{\rho}_a \quad \text{and} \quad \tau' = \tau - \hat{\tau}. \tag{4.15}$$

At each time step, τ' is transformed to spectral amplitudes, from which $\nabla\tau'$ and $\partial_z\tau'$ are obtained by the inverse transform.

The pressure gradient term in (4.7) is now calculated by

$$\rho^{-1}\nabla p = (1 + \mu)^{-1}(\nabla\tau' + \tau\nabla a'), \tag{4.16}$$

and the same in (4.8), but together with g, by

$$\rho^{-1}\partial_z p + g$$
$$= (1 + \mu)^{-1}(\partial_z\tau' + \rho\partial_z a' + \tau'\partial_z\hat{a} + g\mu'), \tag{4.17}$$

where (4.9) has been used in the derivation. Note that a is the log-density of dry air and μ the mixing ratio of the total water substance, as previously defined.

It is significant that the rhs of (4.17) avoids a severe numerical degradation that would occur if the two large terms on the lhs were directly calculated to yield a small residual. When precipitation is present, μ_r is the most prominent contributor to μ', and the last term, $g\mu'$, in (4.17) represents the so-called water loading effect.

The new strategy for evaluating the pressure gradient via spectral transform costs a little more computation time but works extremely well. In fact, we have been able to remove all ad hoc diffusion terms which were once included in the prognostic equations, since no noise occurs that must be suppressed by such means.

d. Hyperbolic transform of mixing ratios

A purely computational problem of *negative* water can occur in any numerical model of finite resolution. In our spectral model, it occurs in sidelobe oscillations due to Gibbs' phenomena. The sidelobes are not the reflection of spectral aliasing or other inadvertent error, but are simply the result of discarding the unresolvable part of would-be continuous spectra. Their amplitudes, in practice, are found to be less than a few percent of the main lobes; and, if left untouched, they normally incur no cumulative or permanent damage to model runs, except for the case of water substance.

Near the edge of a cloud, especially above the cap of a rising convective cell, the predicted mixing ratio, μ or μ_r, may become negative in the sidelobes and cannot be interpreted thermodynamically. When finite-difference models encounter similar difficulties, some propose to redistribute negative values to neighboring grid points, or some others employ the upstream difference scheme to avoid generation of negative values. The definition of a neighborhood in the former is arbitrary, and the scheme of the latter is very dispersive. There are more elaborate schemes to preserve positiveness (e.g., Shchepetkin and McWilliams 1998), which we are not quite ready to adopt.

Another way of coping with the problem is to predict a transformed variable. For example, if $\nu = \ln\mu$ is predicted, the recovered $\mu = \exp\nu$ will always be positive, regardless of Gibbs' phenomena in ν. However, the logarithmic function bends μ at all values; and, in practice, the mean of μ is not well preserved. As a better alternative, we propose a functional transform by one branch of a hyperbola, in which μ is stretched only when it is small enough to be meteorologically insignificant.

Let us consider first a hyperbolic transform and its inverse, defined by

$$\nu = 0.5(\mu - \mu_0^2/\mu), \qquad \mu = (\nu^2 + \mu_0^2)^{1/2} + \nu, \tag{4.18}$$

where μ_0 is a constant (typically 10^{-7}), and a numerical factor 0.5 on the first equation eliminates the necessity of coefficients in the second. This transform is practically linear; that is, $\nu \sim 0.5\mu$, for $\mu \gg \mu_0$. If ν becomes negative, μ will remain positive. Unfortunately, this simple transform is invalid at $\mu = 0$; thus, it cannot be applied to the mixing ratio of condensate. Therefore, (4.18) is slightly modified to extend its validity to $\mu = 0$.

The biased hyperbolic transform and its quasi-inverse are written in terms of two functions, bhyp(μ) and ahyp(ν), which are defined by

$$\nu = \mathrm{bhyp}(\mu) \equiv 0.5[(\mu + \mu_0) - \mu_0^2/(\mu + \mu_0)], \tag{4.19}$$

$$\mu = \mathrm{ahyp}(\nu) \equiv \begin{cases} (\nu^2 + \mu_0^2)^{1/2} + \nu - \mu_0, & \text{if } \nu \geq 0, \\ 0, & \text{if } \nu \leq 0. \end{cases} \tag{4.20}$$

The transform between μ and ν is again linear for $\mu \gg \mu_0$, and bhyp(μ) is valid at $\mu = \nu = 0$. If ν is negative, the strict inverse of (4.19) will find a negative μ but only within a limited range: $-\mu_0 < \mu < 0$. Therefore, the maximum adjustment of negative μ by ahyp(ν) does not exceed μ_0.

The proposed adjustment is admittedly pragmatic but its meteorological significance (or insignificance) may be measured in terms of the potential temperature difference, $\Delta\theta$, between whether the amount of water represented by μ_0 is in vapor or fully condensed. Our typical value, $\mu_0 = 10^{-7}$, yields $\Delta\theta < 3 \times 10^{-4}$ K, which we consider to be small enough. We have made a number of test runs in vigorously convective situations. The results showed no discernible difference between $\mu_0 = 10^{-7}$ and 10^{-8}, while very slight differences were detected in the case of $\mu_0 = 10^{-6}$.

The transform by bhyp(μ) is required only for preparing the initial ν before a model run, and there would be no problem in restricting the initial input of μ to be zero or positive. The prediction is made in terms of ν, and it may run freely positive or negative. Although μ at each time step must be recovered by ahyp(ν) as input to thermodynamic diagnosis, ν itself is untouched, so that the effect of μ adjustments does not accumulate in the predicted ν.

Applying (4.19) to the two variables $\mu = \mu_m + \mu_r$ and μ_r, we may rewrite (4.4) and (4.5) as

$$D_t\nu_r = (d\nu_r/d\mu_r)\rho_a^{-1}[Q_r - \partial_z(\rho_r W)], \tag{4.21}$$

$$D_t\nu = -(d\nu/d\mu)\rho_a^{-1}\partial_z(\rho_r W), \tag{4.22}$$

where $\nu_r = \mathrm{bhyp}(\mu_r)$, $\nu = \mathrm{bhyp}(\mu)$, and

$$\frac{d\nu_r}{d\mu_r} = \frac{(\mu_r + \mu_0) - \nu_r}{(\mu_r + \mu_0)},$$

$$\frac{d\nu}{d\mu} = \frac{(\mu + \mu_0) - \nu}{(\mu + \mu_0)}. \tag{4.23}$$

Actual prediction of ν is performed in terms of its deviation ν' from the background $\hat{\nu} = \mathrm{bhyp}(\hat{\mu})$.

5. Numerical method

a. Conditions for ideal nesting

In order to allow the large-scale environment to interact with convective clouds, the model is configured on horizontally nested domains of varying resolution. In the vertical there is no nesting, but the resolution may be optionally varied with height by the use of a stretched coordinate.

For prediction of a hyperbolic system of equations, nested models have been known for numerical noise that is generated as waves attempt to cross a domain interface. By adopting a nesting strategy, we accept the obvious fact that certain short waves in one domain are geometrically unresolvable in another of a coarser resolution. No numerical scheme can alter this fact. However, it must also be recognized that those would-be-resolvable waves are not necessarily transmissible to the coarse domain. Transmissibility depends on dynamics and is determined by the existence of a matching time-frequency on both sides. It can be improved by accurate numerical methods but never beyond the resolvability. In designing a nesting strategy, therefore, we must observe the following conditions.

1) The gap between resolvable and transmissible waves should be minimized.
2) Nontransmissible waves should not be allowed to reach the interface. If they do, they will be totally reflected, usually as waves in the computational mode with negative group velocities.
3) The computational phase speed of transmissible waves must be identical on both sides of the interface. A mismatch of phase speeds will cause partial reflection.
4) The interface condition for any field variable is simply that its value and spatial derivatives of every order are matched across the interface. Then, provided conditions 2 and 3 are met, the transmissible waves will be oblivious to the presence of the interface.

The harmonic spectral method is ideal in many respects, but it does not accept any boundary condition except for periodicity. There have been proposals (e.g., Tatsumi 1986) for a modified harmonic spectral method which incorporates a few nonperiodic bases to satisfy arbitrary conditions at the exterior boundary of a finite domain, but the idea is not extendable to two-way nesting over multiple domains. A series of Chebyshev functions can also accommodate boundary conditions (Fulton and Schubert 1987), but the nonuniform spatial representation, extremely skewed toward the boundary, makes it a poor choice for atmospheric applications.

Among the gridpoint methods, second-order difference schemes are employed in many nested models, such as Kurihara and Bender (1980), Zhang et al. (1986), Chen (1991), and Grell et al. (1995). However, the dispersion characteristics of second-order schemes are hardly ideal in view of the conditions stated above. If the mesh size is Δx in a fine domain and doubled in an adjacent coarse domain, the threshold wavelength of transmissibility (by the centered scheme with Courant number 0.5) is $11.5\Delta x$; waves shorter than this limit are totally reflected, and longer waves (up to $20\Delta x$, depending on the assumed tolerance level) cause partial reflection. The reflected waves, which are pure noise in the computational mode, can be removed by appropriate filters or damping schemes, but it is more important to narrow the spectral range of nontransmissible waves by employing accurate numerical schemes. This can be achieved by the use of higher-order difference schemes (e.g., Tremback et al. 1987) but necessary studies of interface conditions for nesting have not been undertaken.

b. The SAFER method

The nesting strategy we have adopted is the spectral representation of spatial fields by cubic B-splines, which are assigned one each at equally spaced nodes in a domain and form the basis functions. Any field, represented by a set of amplitudes at the nodes, is continuously differentiable up to the second order, and the third-order derivative is piecewise continuous. The idea was first applied to Global Atmospheric Research Program Atlantic Tropical Experiment data analysis by Ooyama (1987) and further developed as the architectural foundation for domain nesting in prognostic models. The algebraic detail of this numerical method, called the Spectral Application of Finite-Element Representation (SAFER), was described by DeMaria et al. (1992), including the definition of spline-spectral transforms, the low-pass filter built into the transform, the general form of boundary conditions, and the logistics of exchanging data between adjacent domains. While barotropic hurricane track forecasting was the only application discussed by DeMaria et al. the method itself is sufficiently accurate and versatile for application to numerically more demanding problems. The result of a test with a nonlinear flow problem (Straka et al. 1991) is given in appendix C, although this example is in a single domain and does not involve nesting. For the present purpose, a few significant aspects of the method may be noted below.

The size of the nodal interval, Δx, determines the resolution of each domain. As in a finite Fourier series, only the cosine wave has a representation at the Nyquist wavelength, $2\Delta x$. Unlike the Fourier, however, the disparity between cosine and sine lingers on up to about $3\Delta x$ waves, and these short waves should not participate in the spectral representation. Thus, a constraint on the third-order derivatives is included in the least-squares minimization that defines the transform of spatial fields to nodal amplitudes. The constraint has the effect of a low-pass filter with a sixth-order cutoff taper; its spectral response R (translated as for a Fourier filter) is given by

$$R(l, l_c) = [1 + (l_c/l)^6]^{-1}, \tag{5.1}$$

where l is the wavelength in units of Δx and l_c the adjustable cutoff wavelength (defined as the half-response point), which is normally taken to be 2 but may be defined as a function in space.

For wavelengths greater than $3\Delta x$, the phase speed is very accurate provided that the Courant number does not exceed a critical value ($\sim\pi^{-1}$). The threshold wavelength of transmissibility (to a double-spaced coarse domain) is $5.2\Delta x$, and waves longer than $6\Delta x$ are fully transmissible. Therefore, if l_c is gradually increased from 2 to 4 in a narrow zone abutting the interface, all waves approaching the interface are transmitted to the coarse domain without reflection. Thus, the present method meets conditions 1 through 3 quite well; in fact, it does much better than fourth- or even sixth-order difference schemes theoretically could. Furthermore, since spline bases are local, only three nodal amplitudes are needed to exactly satisfy up to three boundary conditions, either homogeneous or inhomogeneous, so that condition 4 can be easily formulated. Thus, the continuity of spatial fields at the interface will be identical to that in the domain interior, assuring the transmission of waves in both ways.

c. Time integration

The time integration is made in discrete time steps, Δt, by the leapfrog method or, alternatively, by the second-order Adams–Bashforth method.[2] For computational stability, either method limits the Courant number approximately to

$$\frac{c\Delta t}{\Delta x}, \qquad \frac{c\Delta t}{\Delta z} < \frac{1}{\pi}, \tag{5.2}$$

where c represents the maximum wave speed possible in the model physics. The atmosphere we consider is compressible and contains acoustic waves as a possible

[2] The so-called lattice separation is often associated with the leapfrog method. This problem in the usual sense of space–time coupling does not occur with our spectral method. However, in marginally saturated areas, water may condense at one step and evaporate at the next; and, on rare occasions, the water-phase oscillation becomes unstable through dynamic feedback. An Asselin (1972) time-filter with a small coefficient (0.1) can prevent instability. The Adams–Bashforth method does not need the Asselin filter, but our comparison tests have not found clear evidence that it is superior to the leapfrog method with the filter.

mode of solution, even though acoustic waves carry very little information of meteorological significance. Thus, if the equations in section 4 are to be explicitly integrated, the size of a stable Δt will be severely restricted by the speed of sound. A number of methods are employed in atmospheric models to abate this acoustic problem. For example, by modifying the physical equations, the anelastic approximation (Ogura and Phillips 1962) eliminates the possibility of acoustic waves, or the quasi-compressibility approximation (Droegemeier and Wilhelmson 1987) slows down their speed; and the split time-level method (Klemp and Wilhelmson 1987) gains efficiency by calculating only the acoustic waves by simpler equations in small time steps.

We have decided to adopt the semi-implicit method. It does not remove acoustic waves, but slows down phase speeds in such a way that they are no longer a factor in determining stability. The method was originally proposed by Robert (1969, 1979) and now widely used in hydrostatic global models (against gravity waves); the first application to a nonhydrostatic model was made by Tapp and White (1976). In adaptation to the nested spectral model, we follow Burridge's (1975) formulation in which the time integration in each domain is split into two steps. In the first step, all the prognostic variables are explicitly predicted by the leapfrog (or Adams–Bashforth) method for Δt that is small enough only for gravity waves and other meteorological modes of solution. The explicit results, then, are ''implicitly'' adjusted in the second step. The required adjustments are determined by solving a second-order elliptic equation with a forcing term that comprises the second-order time difference of predictions at the current (i.e., the explicit step) and two previous time levels. Since the goal is not to precisely calculate acoustic waves but only to stabilize them, the adjustments need to be made only among the velocity components and the dry-air density, leaving the moisture variables unaltered.

In actual calculations, the explicit prediction is made in the geometrical space; the result is transformed to spline amplitudes; and the adjustments are made exclusively in the spectral space of amplitudes. The adjustment equation is actually an algebraic equation that is derived by applying the variational principle to the corresponding equations in the geometrical space. Since no cross differentiation is made in the derivation, there is no need for extraneous boundary conditions on vorticity or divergence. Furthermore, the algebraic equation can be efficiently solved by iterating a one-dimensional solver in alternate directions; two to three iterations in each direction are found to be sufficient. As the result, we have been able to increase Δt tenfold in exchange for a 10% increase in computation time per time step.

Due to the need for an extensive introduction of spectral notation, the mathematical detail of the algorithms is deferred to another paper which will be devoted to our numerical method.

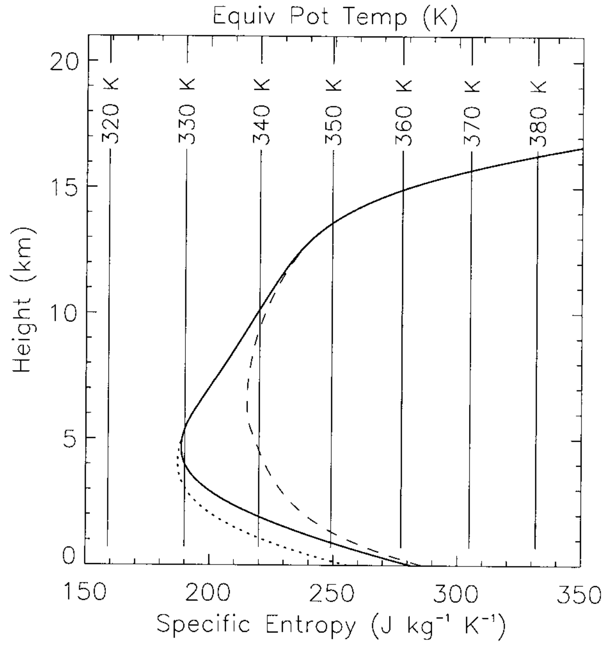

FIG. 1. The assumed background profile of the specific entropy (solid line), which is a slightly humidified version of Jordan's (1958) mean tropical atmosphere for the hurricane season (dotted line). The entropy of saturated air at the same temperature (dashed line) is also shown. For the convenience of traditional interpretation, the diagram is ruled by the equivalent potential temperature (6.1).

6. Single-cell experiments

a. The model setup

The simulated growth of a cloud cell in the two-dimensional vertical plane is discussed in this section. The ground is flat and no rotation ($f = 0$) is assumed. The cloud begins as a warm bubble near the ground and rises by its buoyancy through a horizontally stratified atmosphere, which is initially at rest. The background profile of the specific entropy, s, is shown in Fig. 1. The solid curve is the assumed background, which is a slightly humidified version of Jordan's (1958) mean tropical atmosphere for the hurricane season (the dotted line). The entropy of saturated air at the same temperature is shown by the dashed line, indicating the air below 2 km as potentially unstable if lifted. For the convenience of traditional interpretation, the diagram is also ruled by equivalent potential temperature, θ_e, which is calculated by a simplified definition,

$$\theta_e = 273.15 \exp(s/c_{Pa}). \tag{6.1}$$

The initial disturbance is defined, in terms of temperature deviations, by

$$T' = \Delta T_{\max}[1 + \cos(\pi r)]/2, \tag{6.2}$$

where, for $|x| \leq a$ and $0 \leq z \leq (b + c)$,

$$r \equiv \left[\left(\frac{x}{a}\right)^2 + \left(\frac{z - c}{b}\right)^2\right]^{1/2}, \tag{6.3}$$

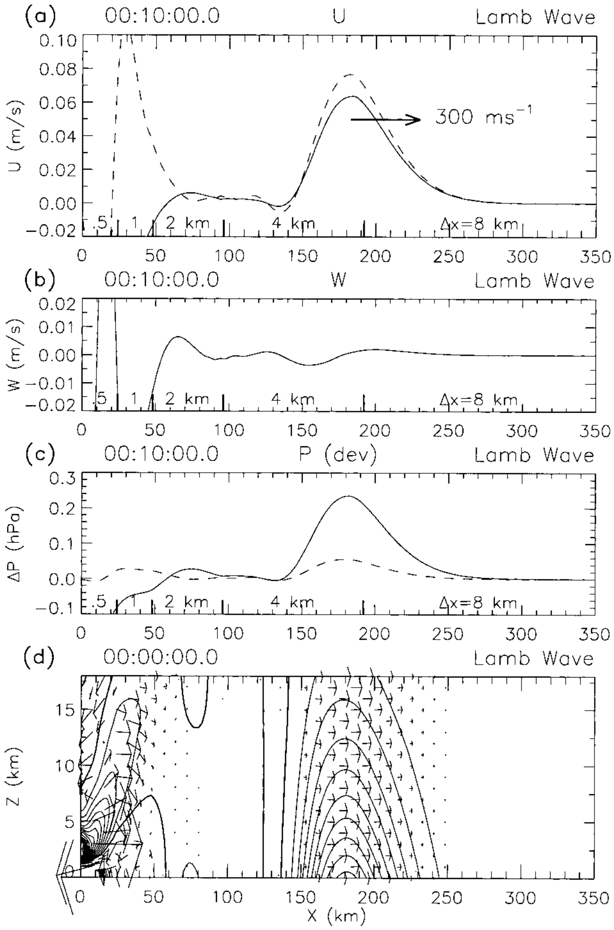

FIG. 2. A propagating Lamb wave, 10 min after its initiation at the origin: (a) u at $z = 0$ (solid) and 15 km (dashed); (b) w at 9 km; (c) pressure variations, Δp, at 0 (solid) and 9 km (dashed); and (d) Δp contours (.025-hPa intervals) and wind arrows in the vertical plane. The longest arrow within the wave is $\sim$0.1 m s^{-1}. The thick tick marks on the x axis indicate the position of domain interfaces, and the resolution of each domain is noted between the marks. Both u and Δp are vertically in phase, and w is very small.

and $a = 16$, $b = 3$, $c = 0.5$, all in km, and $\Delta T_{max} = 3$ K. The relative humidity is not changed in the initial disturbance.

The domain configuration of the model is very flexible. To maintain some order in the presentation, the results shown in this section use the same, concentric nesting to five levels. The innermost domain is in $|x| \leq 24$ km, and the size doubles at the next level of nesting, as is shown in Figs. 1 and 2. The outermost domain extends to $x = \pm 384$ km where periodicity closes the domain. While the domain sizes are fixed, the horizontal resolution varies with each experiment. Thus, Δx of the innermost domain, ranging from 200 m to 4 km, may identify a particular run; and, in any run, Δx of the other domains are outwardly doubled.

The vertical extent of the modeled space is from 0 to 21 km. The vertical resolution is fixed at $\Delta z = 500$ m, except for the case of $\Delta x = \Delta z = 200$ m. A condition $w = 0$ is enforced at the top and bottom boundaries. For other prognostic variables, the second derivatives w.r.t. z are set to zero at the bottom, while both the first and second derivatives are zero at the top.

The time integration employs the leapfrog/semi-implicit combination; in the innermost domain, Δt is 1.25 and 2.5 s for $\Delta x = 200$ and 500 m, respectively, and 5 s for other Δx; and it may be outwardly doubled in the outer domains, although it should be kept under 40 s for which the vertical propagation of gravity waves becomes unstable when $\Delta z = 500$ m.

b. *Propagating waves*

Before focusing our attention on the main event near the origin, we briefly discuss propagating waves in outer domains.

While the background state is hydrostatically balanced, the initial bubble is not, and it explodes like a little bomb, creating acoustic waves. Most of them reverberate between the top and the bottom of the domain and lose identity as recognizable waves. Only one component, known as the Lamb wave, propagates horizontally for a long distance. Figure 2 depicts the wave 10 min after the initiation, located at 180 km from the origin. Thus, the wave has been propagating at a speed of 300 m s^{-1}. The thick ticks on the x axis mark the location of domain interfaces, and Δx for each domain is also noted. The wave has already crossed the interfaces at $x = 24$, 48, and 96 km, and is crossing another at 192 km. Although amplitudes are small, the u and p perturbations are vertically in phase, and w is very small; in an isothermal atmosphere w would exactly vanish.

The rising bubble at the origin also generates gravity waves. The leading wave of the first internal mode is depicted in Fig. 3, at $t = 1$ h and $x = 85$ km. The wave was not fully formed until the bubble rose to the top in about 30 min, so that the propagation speed of the wave is about 50 m s^{-1}. Both the u and p perturbations have opposite signs between the upper and lower levels of the troposphere, while w is maximum at mid levels and lags in the horizontal phase. Thus, the wind field has the appearance of clockwise rotation as it propagates to the right. The wave has already crossed two interfaces, will cross another at 96 km, and is followed by slower gravity waves of higher modes.

It may be noted that our interface condition for nesting is not selectively adjusted to a certain mode or speed of waves, but simply asserts that the order of spatial continuity of fields at an interface is identical to that in the interior of any domain. Thus, it works equally well with acoustic and gravity waves, shown above and with advection, shown later.

c. *The growth of a single cloud*

The growth of a cloud in the 500-m resolution run is shown in Fig. 4, with 12 panels at 5-min intervals for

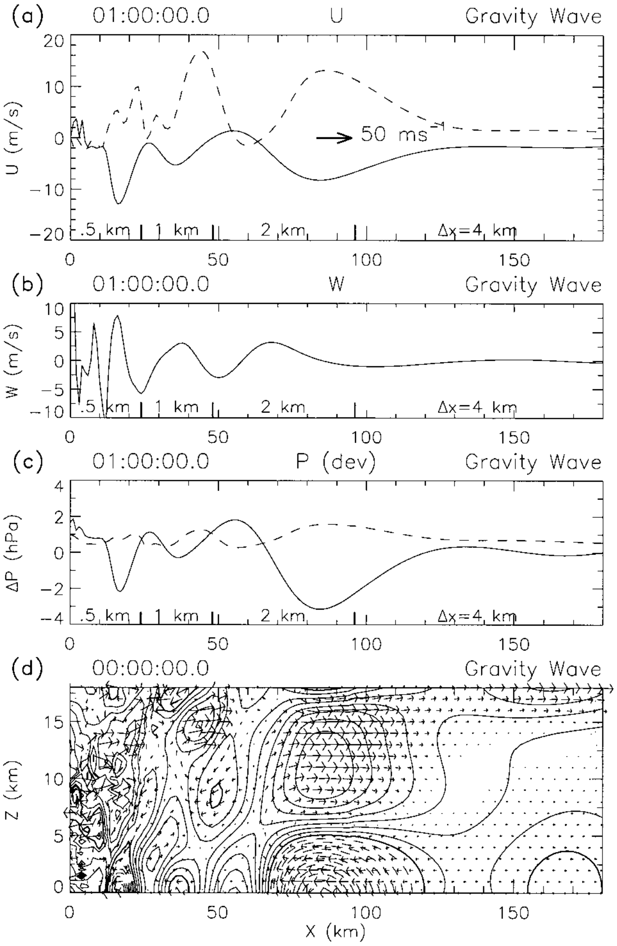

FIG. 3. The leading gravity wave of the first internal mode, at $t = 1$ h, but only 30 min after it was fully formed near the origin. (a)–(d) The same format as in Fig. 1, though the scales are different; e.g., in (d), 0.25 hPa and ~10 m s^{-1}. Both u and Δp are in opposite phase between the upper and lower levels of the troposphere, and w lags by 90°.

1 h. Since the growth is symmetric in x, only the right side is depicted. In each panel, the specific entropy is shown by solid contour lines, the cloudy areas ($\rho_c \geq 0.02$ g m^{-3}) are outlined by a dotted line, and the precipitation water content is in gray shades (7 levels for $\rho_r \geq 0.1$, 0.5, 1, 2, 3, 4, and 6 g m^{-3}). This graphical convention for ρ_c and ρ_r is used in all of the subsequent figures. Wind fields are shown later.

Although the initial perturbation (6.2) is rather broadly defined in x, the rising bubble, as seen in Figs. 4d,e, is very compact, with a sliver of warm[3] air under the cap, and easily penetrates through the cold middle layer. In Fig. 4f the top has reached the tropopause, and a clockwise rotation becomes apparent at the edge of the developing canopy, which spreads farther out and becomes turbulent with time. After Fig. 4h, the thick canopy of ‘‘snow’’ gradually descends; and in Figs. 4k,l, a secondary cell is found near the bottom at $x = 4$ km, forced by a small descending tongue of cold air.

A similar sequence for the 2-km resolution run is shown in Fig. 5. The initial growth is similar but slower; the top rises to the tropopause (in g) 5 min later than in Fig. 4f. By comparison, however, most conspicuous is the absence of a turbulent appearance. The canopy is very thin, because a large portion of condensed water does not rise above 5 or 6 km but falls down early. These differences are analyzed below.

d. Precipitation at the ground

As is known from the linear theory of conditional instability, the vertical acceleration of an unstable parcel or plume depends on its horizontal scale. Such a scale in nonlinear simulations is dynamically determined and affected by the choice of spatial resolution. Figure 6 illustrates such effects by three pairs of diagrams, ($a_{1,2}$), ($b_{1,2}$), and ($c_{1,2}$), for $\Delta x = 1$, 2, and 4 km, respectively. In the first diagram of each pair, the vertical velocity, w (contours), and the precipitation water content, ρ_r (gray shades), both at the center of symmetry, $x = 0$, are plotted against time. The second diagram is the rate of precipitation at the ground, $\rho_r W$, also plotted against time.

The last pair ($c_{1,2}$) is the easiest to interpret. The initial bubble rises slowly; although w eventually reaches its maximum value of 21 m s^{-1} at $z = 10$ km, it remains less than 10 m s^{-1} below 5-km level, and much less at earlier times. The freezing level is about 5 km, and the terminal speed, W, of raindrops is typically 6 to 8 m s^{-1}, so that the precipitation actually falls downward almost as soon as it is formed. Thus, the ground receives a gentle rain continuously after 20 min. (Note that this is more than ‘‘drizzle,’’ since a rate of 50 g m^{-2} s^{-1} is 18 cm of water per hour). Only a small portion of condensed water is lofted above 6 km, due to the increasing w and the decreased W of ‘‘ice-phase’’ precipitation.

Similar interplays of these factors are involved in the other pairs of Fig. 6, but the greater intensity of w produces different precipitation patterns. In ($b_{1,2}$), the ground precipitation does not begin until a lull in w occurs at lower levels around 27 min. In ($a_{1,2}$), it is delayed until $t = 36$ min after the second pulse of updraft; an observer on the ground would see an ominous dark cloud gathering overhead for half an hour and, then, suddenly get doused in a torrential rain. In the runs with $\Delta x = 200$ and 500 m, the onset of ground precipitation is farther delayed and occurs more suddenly than those shown in Fig. 6, although diagrams for these runs are not shown because the rapidity of the w pulsation makes contours too closely packed. The maximum w is 31 and 45 m s^{-1} in (b_1) and (a_1), respectively, and it reaches 60 m s^{-1} in $\Delta x = 200$ m.

[3] Although not technically correct, high or low values of entropy may be referred to as warm or cold, in the sense of (6.1).

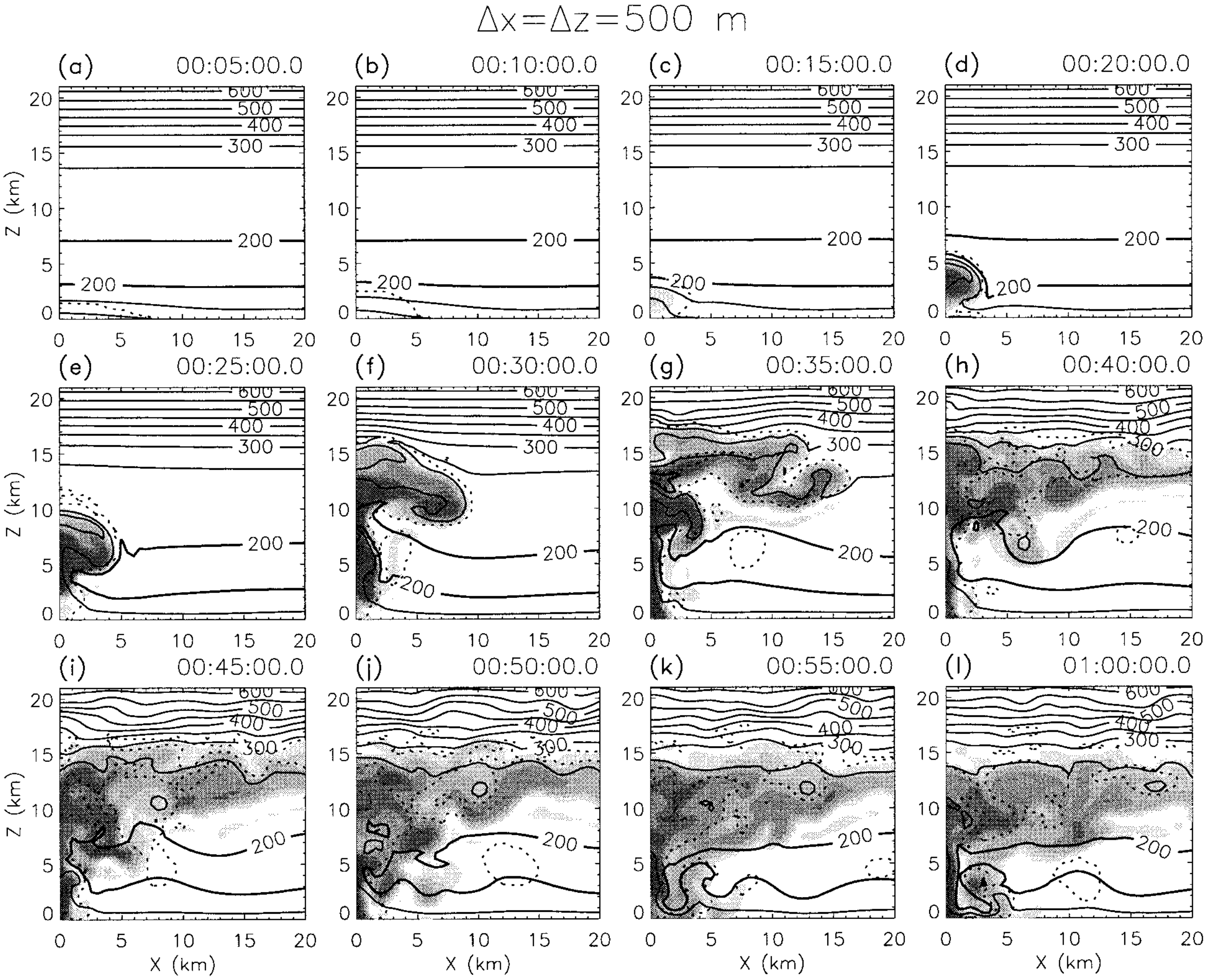

FIG. 4. The growth of a single-cell cloud in the 500-m resolution run shown at 5-min intervals. The time is indicated in the "hh:mm:ss.s" format. Since the growth is symmetric in *x*, only the right-side half is depicted. In each panel, the specific entropy is shown by solid contour lines (with an emphasis on the lowest-level contour), the outline of cloudy areas by dotted lines, and the precipitation water content in gray shades (7 levels for $\rho_r \geq .1$, .5, 1, 2, 3, 4, and 6 g m^{-3}).

e. Wind fields

The wind fields associated with the rising bubble are shown in Fig. 7. Each of the first three rows (Figs. 7a–c) for $\Delta x = 0.5$, 1, and 2 km, contains three panels at $t = 30$, 35, and 40 min, while the panels in the last row (Fig. 7d), for $\Delta x = 4$ km, are at $t = 45$, 50, and 55 min, due to the slow rate of growth. In each panel, the precipitation water content is shown in shaded gray (as in previous figures), the cloud areas are outlined by a solid curve, and the wind vectors in the vertical plane are shown by arrows. The direction of the arrows is correctly adjusted for the scales on the *x* and *z* axes, while their length is not linearly but only monotonically related to the speed in order to accommodate large variations in a tight space.

In all the cases, a rotary circulation develops at the edge of a mushroom-shaped canopy of cloud that is associated with the formation of the first gravity wave shown in Fig. 3. In the lower resolutions, Figs. 7c,d, the flow is largely laminar; and the main circulation splits into two parts, the rising upper part and the rain-loaded lower part. In the higher resolutions, Figs. 7a,b, the circulation is far more complex, reflecting interactions between the initial buoyancy, gravity waves, and precipitation; the vertical motion even at the center is not simply up or down, and the flow breaks up into smaller eddies especially in the spreading canopy.

This trend toward complexity is depicted in Fig. 8 for $\Delta x = \Delta z = 200$ m in three panels, (a_1) to (a_3), at $t = 31$, 33, and 35 min. The wind vectors are plotted only on the right side of each panel to afford an unobstructed view of condensed water on the left. Due to reduced fall speeds, the ice-phase condensate is a good tracer of delicate flows in the canopy.

In (a_1), a pair of mushroom-shaped protrusions has developed on the top of the main canopy; and the ro-

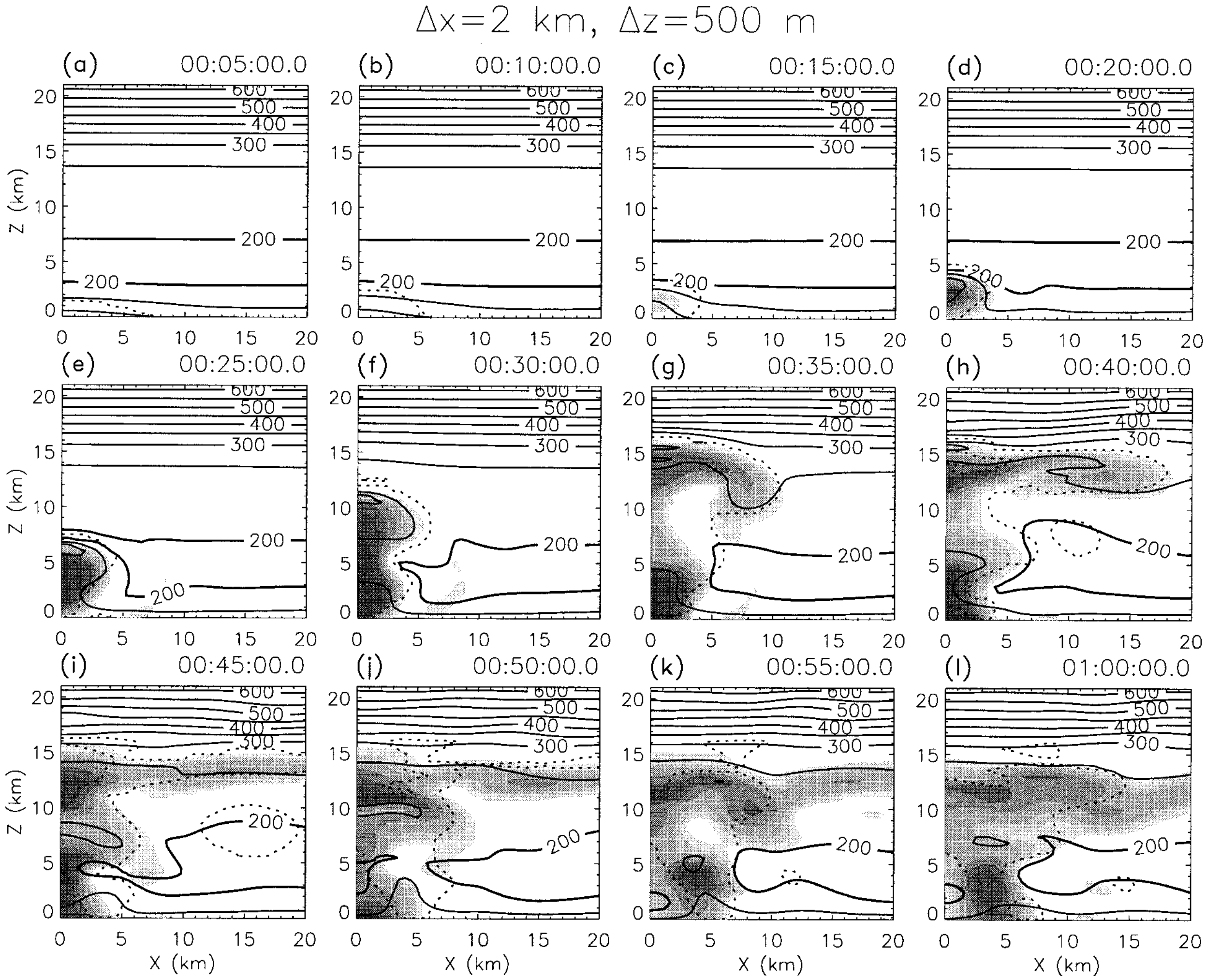

FIG. 5. The same as in Fig. 4, but for the 2-km resolution run.

tation at the outer edge of the canopy is concentrated in a mamma-like hanging protrusion. In (a_2), the rotary circulations associated with the little mushrooms grow stronger, intensifying the narrow downdraft between them (at $x = 0$), while the large canopy almost splits into two parts on each side with two hanging protrusions that rotate in the same direction. In (a_3), only 4 min after (a_1), the entire canopy is a mass of small eddies. The behavior of the second pulse of the updraft at the center of symmetry is also interesting. In (a_1), it is stopped at $z = 7$ km, meeting a downdraft from above, and splits sideways in (a_2) and (a_3), generating its own eddies.

Grabowski and Clark (1991) have discussed the cloud-top instability that generates eddies resembling those in Fig. 8, although only one mushroom grew at the center. In their model, the anelastic approximation was used, the cloud did not precipitate, and the spatial resolution was typically 5 m. We are quite tempted but have not yet run our model at such a high resolution.

f. Asymmetry, natural and artificial

The narrow central downdraft at the top and the collision of the up- and downdrafts in the middle, both in Fig. 8, are singular events due to the assumed strict symmetry. In contrast, the results of two asymmetric simulations are shown in Fig. 9: in Fig. 9a, a weak vertical shear, 5 m s^{-1} per 10 km of height, is assumed in the initial state; in Fig. 9b, there is no shear but the initial bubble is placed exactly at the interface of two domains in such a way that $\Delta x = 200$ m on the positive side of x and 400 m on the negative side. Otherwise, both should be compared with Fig. 8 (a_2).

In Fig. 9a with shear, the two little mushrooms are slanted and no sharp downdraft is found between them; and the collision of the up- and downdrafts at 7 km is diffused. In Fig. 9b the case of interface straddling, only one of the little mushrooms grows at the top, and the opposing drafts in the middle slide past each other. Apart from these details, the general appearance of the two

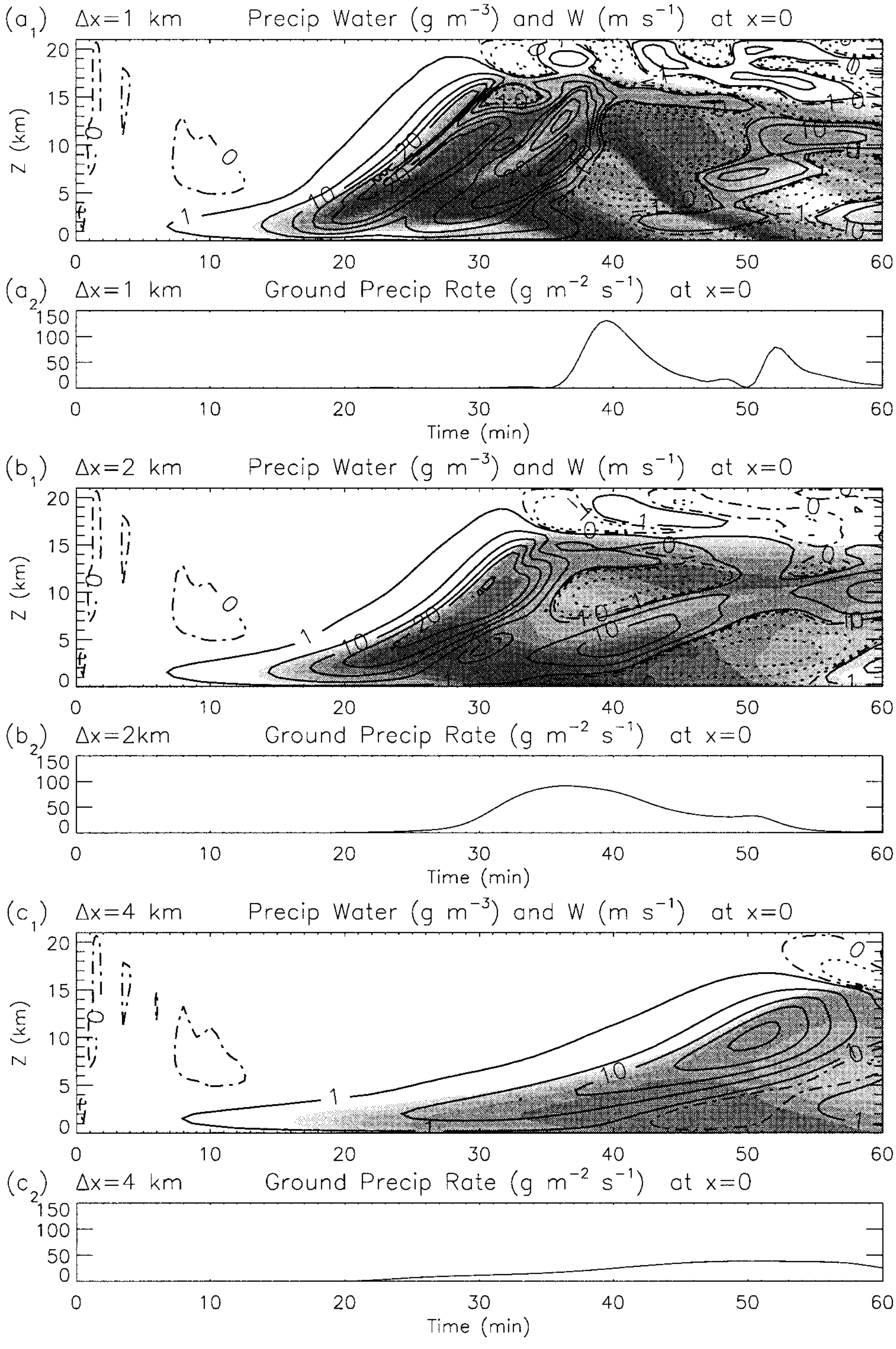

FIG. 6. The vertical velocity (contours) and precipitation water content (gray shades) in (a_1), and the precipitation rate at the ground in (a_2), all at the center x = 0, are plotted against the time for the 1-km resolution run; ($b_{1,2}$) and ($c_{1,2}$) are the same but for the 2- and 4-km runs. The contour levels are 1, 5, 10, 15, 20, 30, and 40 m s^{-1} for positive w but dotted for negative, and 0 is chained. The shading levels are the same as in Fig. 4.

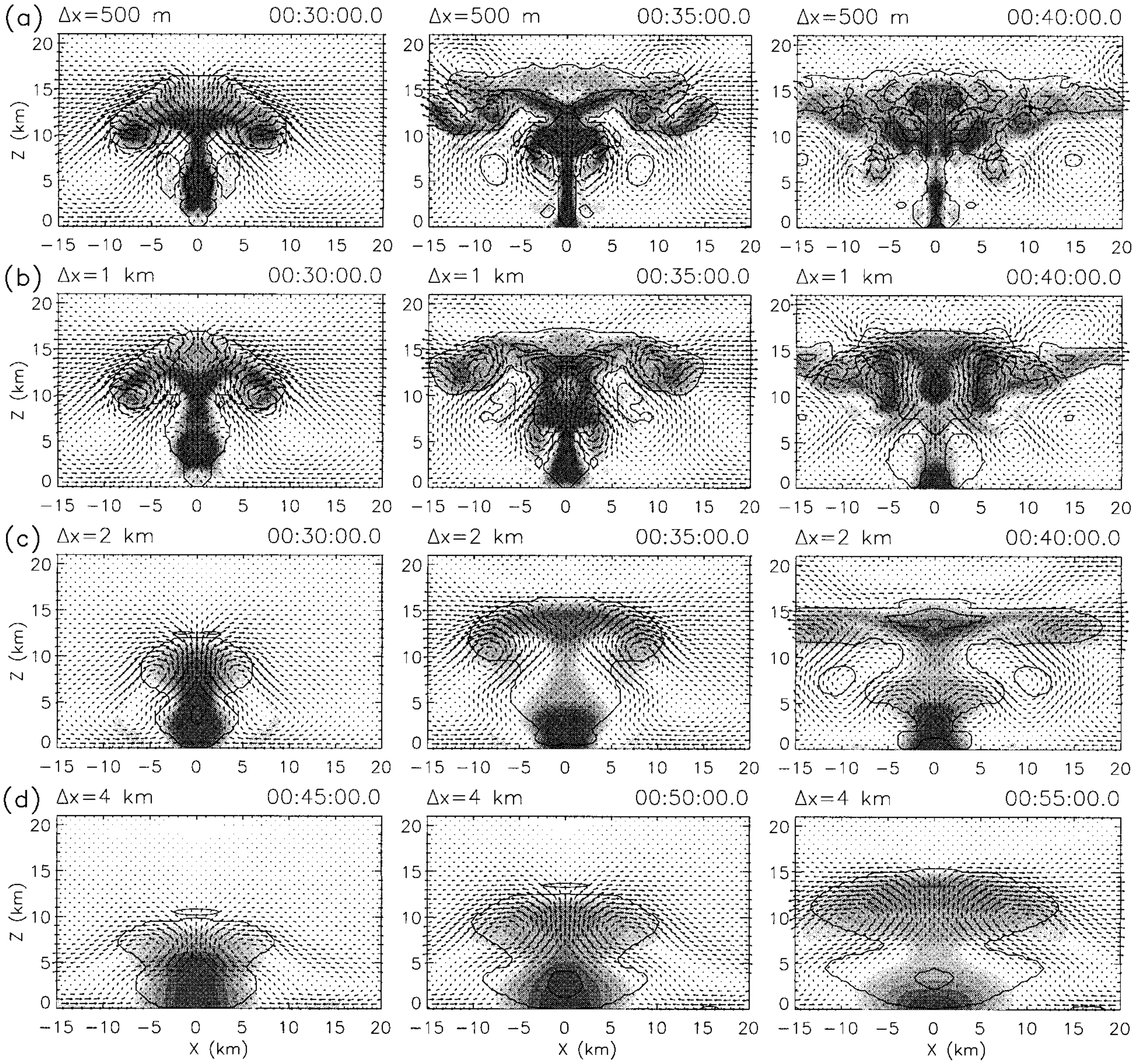

FIG. 7. The winds (arrows) associated with the rising bubble for the runs with (a)–(d) Δx = 0.5, 1, 2, and 4 km, respectively. The three panels in each of the first three rows are at t = 30, 35, and 40 min, but those in the last row are at t = 45, 50, and 55 min due to the slow rate of growth. The direction of the arrows is correctly adjusted for the graphic scales of the axes, while their length is not linearly but only monotonically related to the wind speed. The condensate distributions are also shown as before.

results, including the degree of asymmetry, is quite similar.

As a matter of fact, the similarity is fortuitous, since the asymmetry in Fig. 9a is due to a natural cause while that in Fig. 9b is an artifact of modeling. However, the latter is not a simple numerical problem such as computational dispersion, which is practically absent in the present model. It is rather a fundamental problem of the finite resolution that places a limit on the realizable extent of dynamics in a numerical model. Earlier in this section, the dynamic effects of resolution were examined in separate runs. Fig. 9b demonstrates the degree of inevitable distortion that occurs when the resolution jumps in the midst of a severe convective event.

7. Squall line experiments

a. Anatomy of a simulated squall line

Squall lines have been a subject of extensive studies through observations and models. [See, e.g., Rotunno et al. (1988), or Fovell and Tan (1998) for references]. Since our goal is not to open new ground in this well-cultivated field but rather to test the model, a very simple

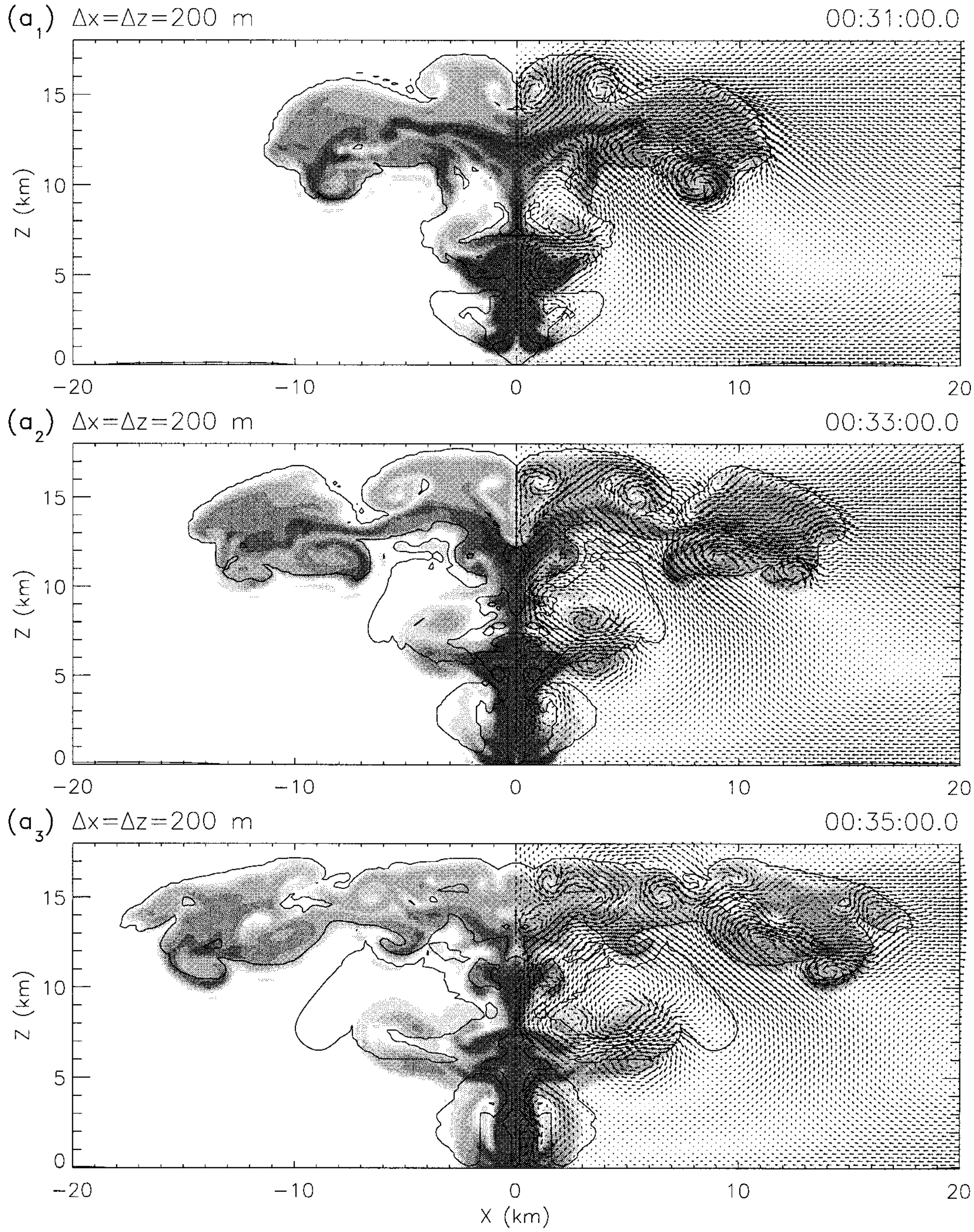

FIG. 8. Enlarged views of the wind and condensate distributions for the 200-m resolution run, at $t = 31$, 33, and 35 min. The winds (arrows) are plotted only on the right side to afford an unobstructed view, on the left, of delicate swirls of condensed water (cloud outlined, precipitation shaded).

setup has been chosen for our experiments. We assume an initial wind profile in the form of

$$U(z) = U_0 \tanh(z/z_{sc}), \tag{7.1}$$

where $U_0 = 10$ m s^{-1} and $z_{sc} = 1$ km, unless otherwise specified. Thus, the atmosphere is in uniform motion above approximately 2 km, and the vertical shear is limited in the shallow layer below. To start convection, the initial disturbance (6.2) is assumed again at $x = 0$. The background stratification is also the same as given in Fig. 1.

The configuration of nested domains is also similar to the earlier one, but each nested domain is twice as wide, slightly off-centered, and on a relative x coordinate translating at the constant speed U_0. Specifically, the innermost domain lies within (−24, 72) km at $t =$

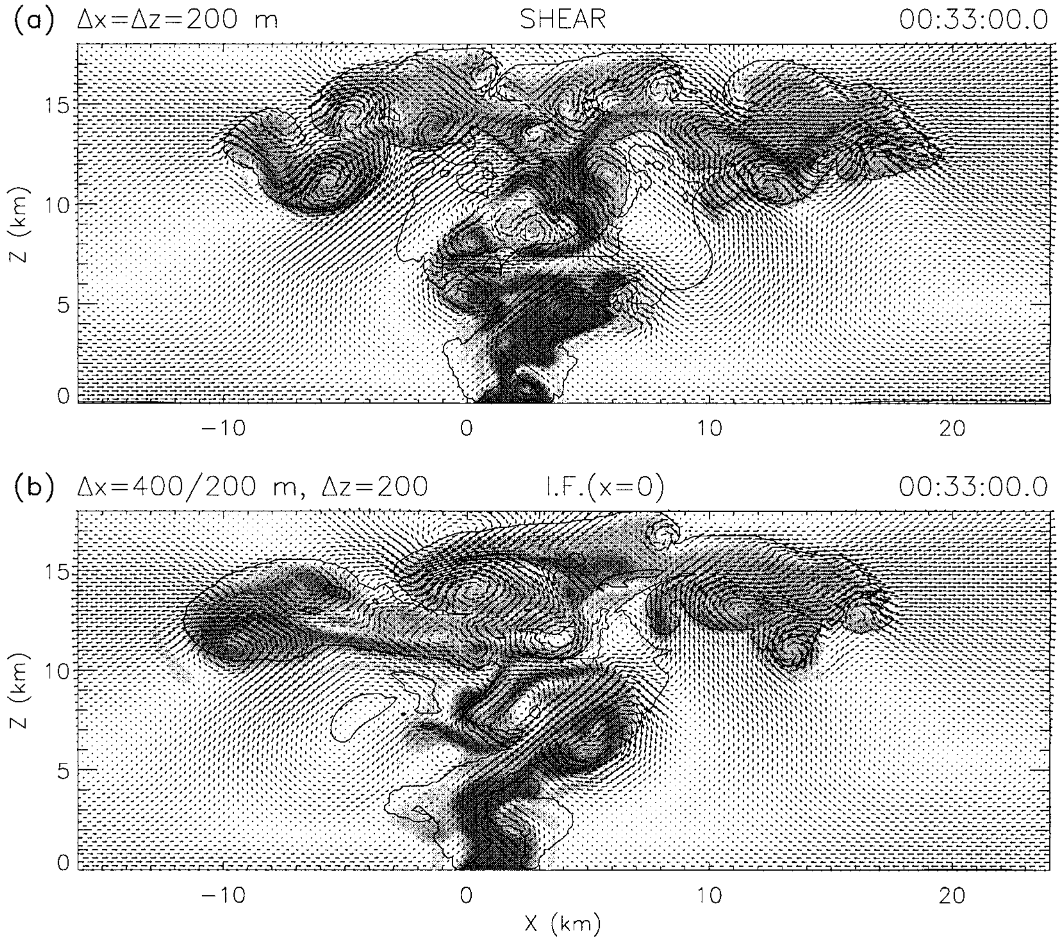

FIG. 9. Asymmetry developed in two modified runs, shown at t = 33 min. (a) A weak shear, 5 m s^{-1} per 10 km of height, is assumed in the initial state of a 200-m resolution run. (b) No shear but the initial bubble is placed exactly at the interface of two domains in such a way that Δx = 200 m on the positive side of x and 400 m on the negative side.

0, will be within (12, 108) km after 1 h, and so on. All the outer domains translate at the same speed. The fifth and periodic outermost domain is 1536 km wide, so that even the fastest gravity wave will take 8.5 h to come around to affect the central area of interest.

A snapshot of the well-organized squall line at 5 h, 50 m in the 500-m resolution run is shown in Fig. 10a. The cloud areas (thin solid lines), precipitation (gray shades) and specific entropy (medium and heavy solid lines) are shown in the same manner as in earlier figures, but the plotted winds (arrows) are relative to the moving coordinate (by subtracting U_0). The x axis is labeled in the true distance from the point of the initial disturbance, and the interface originally at x = 72 km is presently at 282 km, where the resolution changes from 500 m on the left to 1 km on the right. The squall system has been running mostly within the moving, innermost domain but is now overtaking the interface. The vertical profiles of u (velocity) and s (entropy) are shown in Figs. 10b, c, respectively, at x = 260, 290, 320, and 330 km, each marked by a triangle in Fig. 10a. For reference, the initial profile of either u or s is also shown by a dash–dot line. The propagation speed of the system at this time is 19 m s^{-1}.

From Fig. 10a and (c_{1-3}), it is evident in the precipitating area that a shallow wedge of cold air (cooled by up to 7 K in temperature) has accumulated above the ground. A jet of the cold air with a peak at z = 2 km is found in (b_1); it descends to the ground (b_2) and accelerates to a speed greater than 30 m s^{-1} in (b_3) as its depth decreases. Beyond the leading edge of this gust front at x = 322 km, no sign of the gust is found in (b_4), and the entropy profile in (c_4) is hardly modified from the initial state. The advancing cold wedge lifts the hitherto undisturbed air and initiates incipient cloud cells, of which some may fizzle but many grow into mature cells and join the main body of the convective system. The entropy maxima in (c_{1-3}) are the signature of those rising cells that have been left behind the advancing cold air.

At the top of the system, $z \sim$ 11 to 14 km, the downshear outflow of 20 m s^{-1} carries the precipitating cirrus

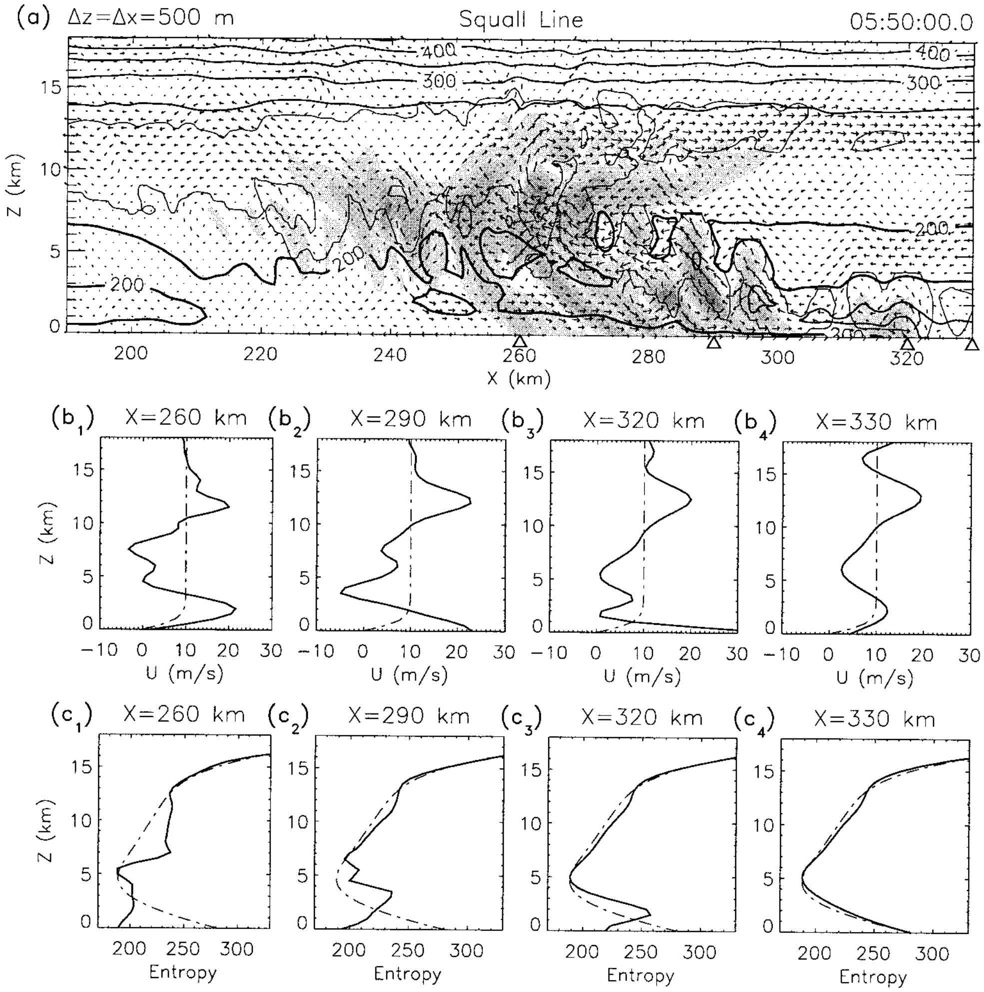

FIG. 10. A snapshot of the well-organized squall line at 5 h 50 m in the 500-m resolution run. (a) The cloud areas (thin outlines), precipitation (gray shades), and specific entropy (solid lines, with an emphasis on the lowest-level contour, 200 J kg^{-1} K^{-1}), and the winds (arrows) relative to the constant wind aloft (U_0). (b) The vertical profiles of u velocity and (c) s (entropy) at the four points of x, each marked by a triangle in (a). For reference, the initial profile of either u or entropy is also shown by a dash–dot line.

canopy forward, while the weaker upshear outflow leaves a long trailing cirrus canopy behind the system. The flow at midlevels is varied; it enters the system from the front, is partially caught in convective updrafts and downdrafts, and exits through to the rear.

The pressure field (not shown) contains high-frequency small-scale fluctuations, reflecting the continual but intermittent activities of numerous cells. Apart from these fluctuations, the surface pressure under the system shows a conspicuous high plateau of $p' \sim 2.5$ hPa between $x = 250$ and 320 km with a slight average gradient which is consistent with the acceleration of the surface wind.

b. Generation of squall lines

Once a simulated disturbance gets its various parts organized in a certain configuration, such as shown in Fig. 10, it becomes a self-perpetuating system as a squall line. On the other hand, the way such organization develops from the assumed initial bubble is a process that requires a favorable combination of many factors. By setting the evaporation rate of precipitation to zero, we can confirm the essential role of evaporative cooling in the generation of a squall line. However, if the evaporation rate is increased without adjusting the fall speed of precipitation, the cooling takes place at wrong places for the creation of cold air above the ground. The preexistence of a low-level wind shear favors a well organized squall line, especially its maintenance after formation. However, the role of shear in the formation is rather ambivalent; a propagating line of convective clouds can form without preexistent shear; and a strong shear may delay, or even prohibit, the organizing process.

To examine this question about the role of shear, a

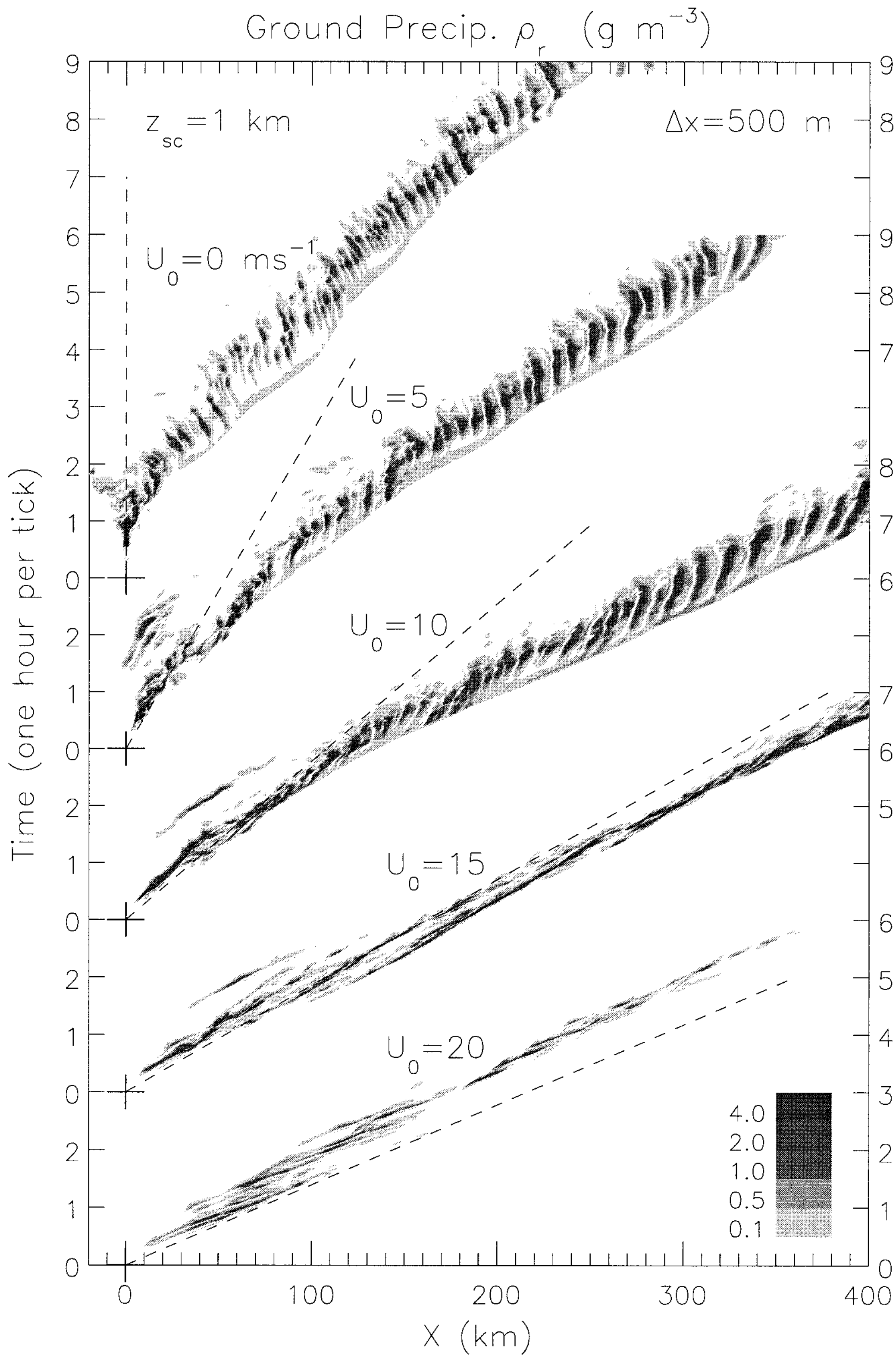

FIG. 11. The precipitation water content ρ_r (g m^{-3}) at $z = 0$ is portrayed in gray shades as a function of x and t for five cases of $U_0 = 0$, 5, 10, 15, and 20 m s^{-1}. The time origin for each case is offset to avoid overlap. The trace of a point moving at the speed of U_0, starting at the origin of each case, is shown by a dashed line.

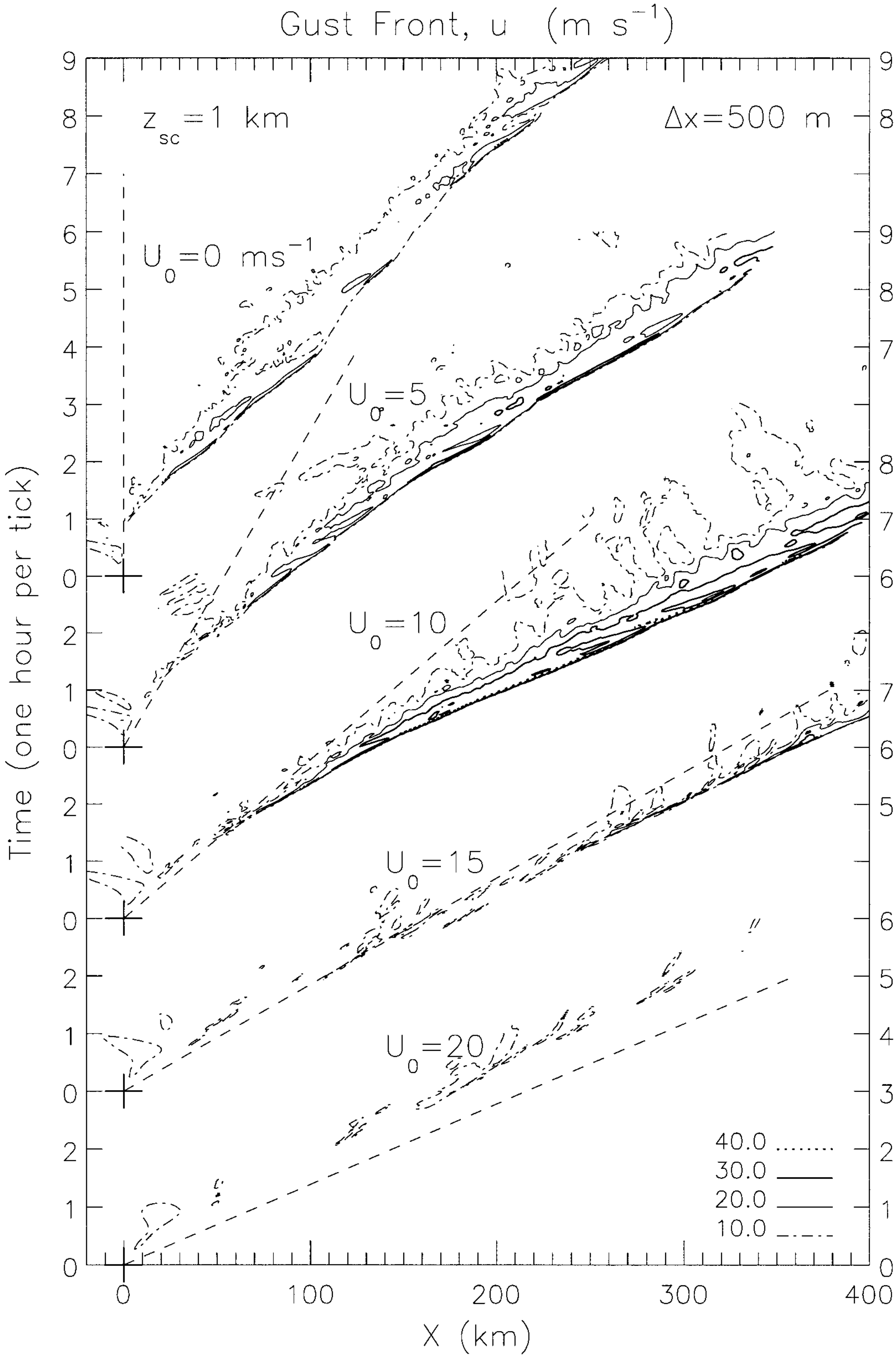

FIG. 12. The horizontal wind speed u (m s^{-1}) at $z = 0$ is contoured as a function of x and t for the same cases as in Fig. 11. The contour levels are chosen for a clear depiction of the gust front.

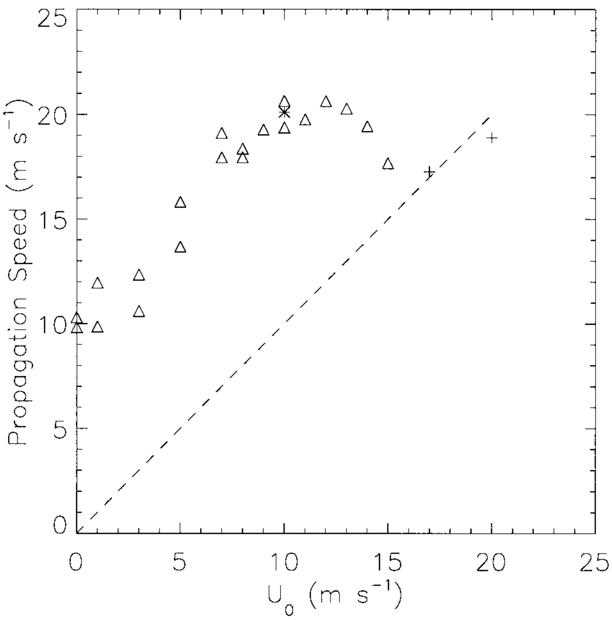

FIG. 13. The propagation speeds of simulated squall lines are plotted against U_0. Triangles indicate the speeds of well-established gust fronts, except that it is for local gusts in the case of no shear. A single asterisk at U_0 = 10 is for the special case of z_{sc} = 2 km. Crosses indicate the speeds of drifting clouds when no gust front is formed.

series of experiments has been conducted in which U_0 of (7.1) is varied from 0 to 20 m s^{-1} while z_{sc} is fixed at 1 km (except for one case mentioned later). This choice of U_0 (the wind aloft) as the primary designator of the boundary shear, rather than the vertical gradient of $U(z)$, follows the convention adopted by Fovell and Ogura (1989, hereafter FO89), although our U_0 does not numerically correspond to their Δu due to the use of different profile functions. The configuration of nested domains is similar to the case discussed in the previous subsection, but the translation speed of domain interfaces has been adjusted for each case in order to keep, as much as possible, the propagating activities within the innermost domain of 192-km width.

The results are summarized in Fig. 11, in which the precipitation water content ρ_r at $z = 0$ is plotted in gray shades as a function of x and t for five cases of U_0 = 0, 5, 10, 15, and 20 m s^{-1}. The time origin for each case is offset to avoid overlap. The horizontal wind speed u at $z = 0$, also a function of x and t, is contoured in Fig. 12 for the same cases. The contour levels are chosen for a clear depiction of the gust front. The trace of a point moving at the speed of U_0, starting at the origin of each case, is shown by a dashed line.

In the case of U_0 = 0, the cold pool of air accumulates under the initial cell for the first hour and then starts spreading out at a speed of about 10 m s^{-1}, initiating weak convective cells on its path in a quasi-periodic fashion. The wind u locally exceeds 20 m s^{-1}, but such episodes are intermittent and do not attain the structure of a gust front. Nevertheless, the cloud system represents a clearly defined line of passing showers.

The tendency to form a lasting gust front is enhanced by an increased U_0, but only to a certain limit. In the case of U_0 = 5 in Fig. 12, a continuing zone of $u >$ 20 m s^{-1} is formed behind the rapidly advancing front after t = 3 h. In the case of U_0 = 10, a zone of $u >$ 30 m s^{-1} develops behind the front, and the peak values exceed 40 m s^{-1} just at the front. The precipitation patterns in Fig. 11 indicate regular regeneration of intense new cloud cells in these cases. The trend appears to be reversed at U_0 = 15; although new cells are haphazardly initiated, they simply drift with the wind aloft for the first 5 h, leaving a passive wake of cold air behind them. A weak gust front is eventually formed after 6 h, however. In the case of U_0 = 20, there is no such possibility since convective activities cease after 6 h.

The propagation speeds of simulated squall lines for various U_0 are depicted in Fig. 13. A triangular symbol indicates the speed that is measured by the slope of a gust front in (x, t) plot after it is well established. The case of no shear is included in this category since it appears to be a smoothly connected limit of sheared cases. Two symbols plotted for the same value of U_0 indicate a degree of uncertainty either in the speed itself or in the way of measurement. In spite of this uncertainty, however, the propagation speed seems to reach a maximum at approximately 21 m s^{-1} between U_0 = 10 and 12.

At U_0 = 17 and 20, a "+" symbol indicates the speed of drifting clouds, since no gust front or squall line has formed. It was reported by FO89 that "storms" (squall lines) also failed to form for $\Delta u >$ 22.5 when the model simulation was started from an initial bubble, but that the storm continued to propagate, if Δu was gradually increased from 22.5 to higher values after the storm was established at the low value. Thus, their 22.5 appears to correspond to our threshold at U_0 = 15. If we had employed a similar maneuver to increase U_0 during a run, we might have found squall lines propagating at higher speeds than 21 m s^{-1}. Then, the present maximum in Fig. 13 and a slight irregularity found in a similar diagram (Fig. 2) of FO89 may be related phenomena, although many differences in the experimental designs make such a comparison imprecise.

The depth of the sheared layer is one such difference; it is 2.5 km for a linear wind profile in FO89. In order to reduce the gap, we have conducted one experiment with z_{sc} = 2 km and U_0 = 10 m s^{-1} for our hyperbolic-tangent profile. In this experiment, an initial gestation period lasts for 6 h with haphazard convective activities before a well-organized squall line emerges. When it is finally established, however, the propagation speed is found to be nearly identical to the speed in the case of z_{sc} = 1 km, as shown by an asterisk in Fig. 13, sug-

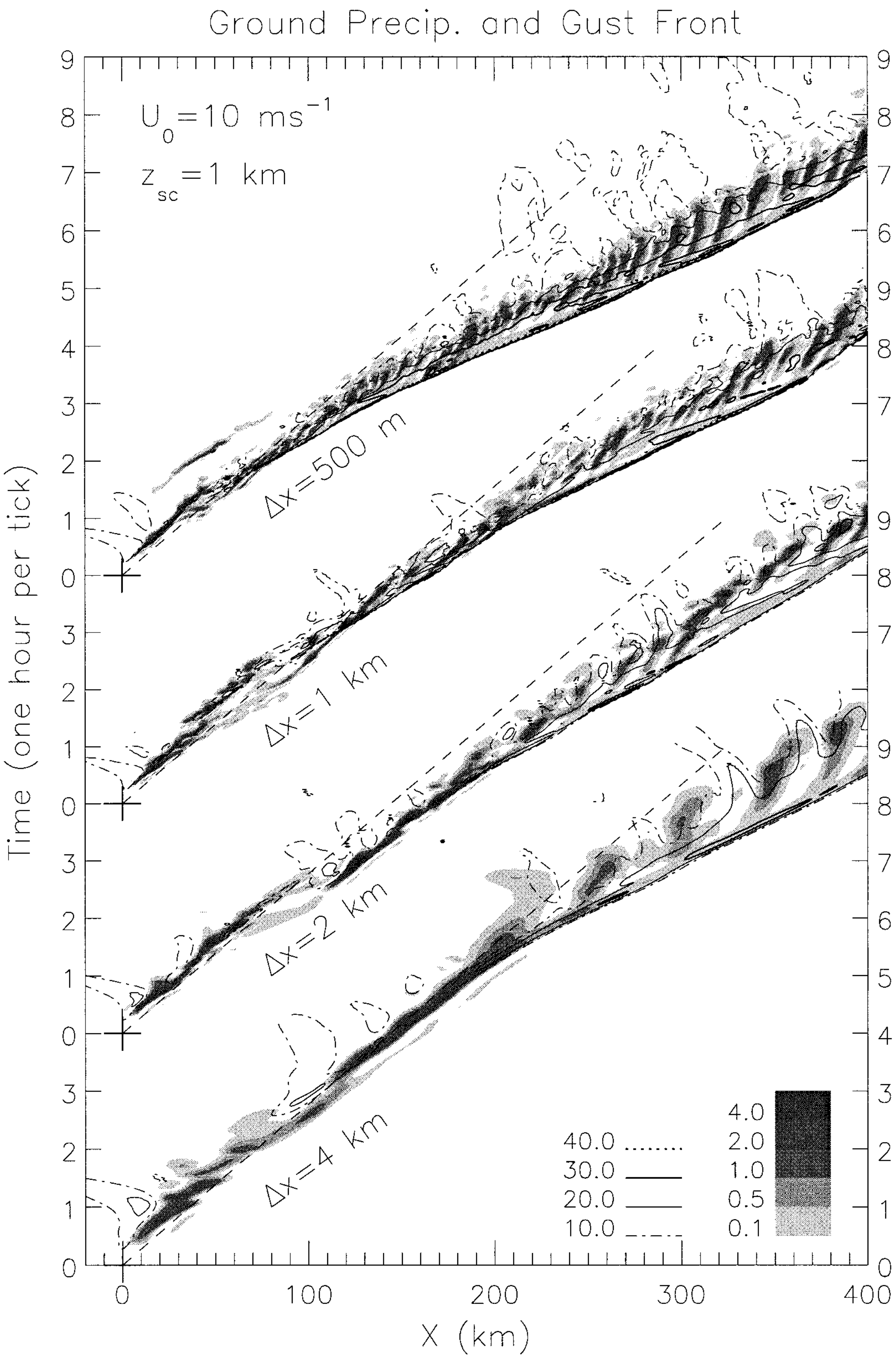

FIG. 14. The effects of spatial resolution on the simulated squall line with U_0 = 10 are demonstrated for Δx = 0.5, 1, 2, and 4 km, in the same format as Figs. 11 and 12, but the wind contours are now superposed on the precipitation.

gesting that the depth of the sheared layer is not a sensitive factor in determining the speed of a mature squall line.

The effects of spatial resolution on the simulated squall line with $U_0 = 10$ are demonstrated in Fig. 14, for $\Delta x = 0.5$, 1, 2, and 4 km. The contour lines of horizontal winds are now superposed on the precipitation in gray shades. As the resolution becomes coarser, the gust front takes more time to develop and attains lesser intensity, although the propagation speed remains in the range of 18 to 20 m s^{-1}. The precipitation patterns are more sensitive to the resolution. Especially in the case of $\Delta x = 4$ km, the formation of new cells is infrequent and each cell is extremely broad.

Weisman et al. (1997) presented similarly broad structures of squall lines, simulated in various resolutions from 1 to 12 km. In their experiments, an initially assumed cold pool of air initiates convection, while, in the present experiments, the cold pool has to be created by convection. We do not know at this time whether or not a squall line can bootstrap itself with 12-km resolution.

8. Concluding remarks

We have proposed a direct and consistent application of dynamic and thermodynamic principles, in conjunction with parameterized microphysics, for modeling the moist, convective atmosphere. A two-dimensional model has tested the theoretical proposal, utilizing a versatile and accurate spectral method based on a cubic-spline representation of the spatial fields. In order to allow a wide range of scale interactions, the model is configured on multiply nested domains of outwardly decreasing resolution, with noise-free, two-way interfaces. The semi-implicit method provides efficient time integration for the nested spectral model.

Tests have been conducted for the growth of single-cell clouds and for the generation of self-sustaining multicell squall lines, both in various spatial resolutions. While the results favorably compare with those found in the literature, they also pose a question about the resolution-dependent interplay between the dynamics and the parameterized microphysics.

The Kessler-type parameterization with an assumed drop-size distribution may not be realistic for every possible occasion, and there is a range of uncertainty as to the choice of coefficients as well as form. Nevertheless, the microphysics in micron to millimeter scales are clearly separated from the smallest scale (perhaps a meter) that a dynamic model of the atmosphere may deal with. In this regard, the parameterization is independent of the model resolution. On the other hand, the dynamics, especially the vertical motion in a conditionally unstable atmosphere, is highly dependent on the resolution, affecting the generation and distribution of precipitation.

Within the limited scope of our experiments, the resolution of $\Delta x = 1$ km or less, or marginally 2 km, is needed for realistic simulations of precipitating clouds. If Δx had to be 4 km or greater, a modified parameterization adjusted to the resolution of the dynamics might perform better, though it would be a murky idea regressing back toward the parameterization of whole clouds. On the other hand, the need for high resolution also depends on the specific goals of the model; coarser resolution may be tolerated, for example, if the convection is the result of other dynamic forcing mechanisms in a nearly moist-neutral atmosphere.

Although omitted in this paper, we have been working on the parameterization of eddy fluxes in the atmospheric boundary layer. The implementation of the surface layer, based on the Monin–Obukhov similarity theory and observationally deduced profiles (e.g., Högström 1988), is a mathematical problem of solving the flux equation. However, the parameterization of the mixed layer is a harder problem; one can adopt one proposal out of hundreds in the literature but will not know its adequacy until it is tested in a particular model for a specific goal. Furthermore, in convectively disturbed conditions, the explicit eddies generated by a model and those implicitly assumed in a parameterization tend to overlap in scales, raising the question of consistency.

The spectral method does not suffer truncation errors in the usual sense of the gridpoint method. However, since not all the possible functions in space belong to the limited class of functions spanned by the chosen spectral bases, the spectral method incurs representation error. In order to abate the problem, a low-pass filter with a sharp cutoff taper is built into our spline-spectral transform. The filter apparently takes care of the small-scale numerical problem associated with the nonlinear spectral cascades, and produces numerically accurate solutions within the resolvable scales. Therefore, although we have entirely avoided the controversial subject of parameterizing the subgrid-scale turbulence, the model can be utilized to study the physical significance of such parameterization, dissociated from its customary role as a computational facilitator.

The theoretical foundation, as well as the numerical method, is extendable to three spatial dimensions, and the construction of a 3D model is contemplated.

Acknowledgments. The author would like to thank Dr. H. E. Willoughby and the late Dr. S. L. Rosenthal for the administrative support of this work, and George Soukup for improving the manuscript. The helpful comments and suggestions from Wayne Schubert, Scott Hausman, and Matt Garcia of Colorado State University are also greatly appreciated. This work was supported in part by a grant of HPC time from the Arctic Region Supercomputing Center, and also from the TACOM-TARDEC HPC Distributed Center.

APPENDIX A

Microphysics Parameterization

The parameterization formulas by Klemp and Wilhelmson (1978), after conversion of the dimensional constants to SI units, are adopted for our experiments, with a modification of the fall speed W by a temperature dependent factor, f_{ice}, when the temperature is below $T_0 = 273.15K$:

$$W = -14.164\rho_r^{0.1364}(\rho_{a0}/\rho_a)^{0.5}f_{ice}, \tag{A.1}$$

where the density variables are in kg m^{-3}, and

$$f_{ice} = \begin{cases} 0.2 + 0.8\ \mathrm{sech}\left(\dfrac{T_0 - T}{5.0}\right), & \text{if } T < T_0 \\ 1.0, & \text{if } T \geq T_0. \end{cases} \tag{A.2}$$

The rates (kg m^{-3} s^{-1}) of the autoconversion Q_{auto}, collection Q_{col}, and evaporation Q_{evap}, are specified by

$$Q_{auto} = 0.001(\rho_c - 0.001\rho_a), \tag{A.3}$$

$$Q_{col} = 2.20\rho_c(\rho_r/\rho_a)^{0.875}f_{ice}, \tag{A.4}$$

$$Q_{evap} = \frac{f_{vent}\cdot\{\rho_v^*(T) - \rho_v\}\rho_r^{0.525}}{\{2.03\rho_v^*(T) + 3.337/T\}\times 10^4}, \tag{A.5}$$

$$f_{vent} = 1.6 + 30.39\rho_r^{0.2046}(f_{ice})^{1.5}, \tag{A.6}$$

where ρ_v^* denotes the saturation vapor density, and f_{vent} is the ventilation factor. These rates are individually set to zero if negative. Since W is implicitly involved in the formulas for Q_{col} and f_{vent}, these are also modified by f_{ice}.

The net production rate (or evaporation if negative), is given by

$$Q_r = Q_{auto} + Q_{col} - Q_{evap}. \tag{A.7}$$

APPENDIX B

Thermodynamic Functions

The entropy functions defined in O90 are listed below in present notation, replacing the original symbols, ξ and η, by ρ_a and ρ_m, respectively. For state 1, with no condensate,

$$S_1(\rho_a, \rho_m, T) \equiv \rho_a s_a + \rho_m s_m^{(1)}, \tag{B.1}$$

and for state 2, with saturated vapor,

$$S_2(\rho_a, \rho_m, T) \equiv \rho_a s_a + \rho_m s_m^{(2)}, \tag{B.2}$$

where

$$s_a \equiv c_{Va}\ln(T/T_0) - R_a\ln(\rho_a/\rho_{a0}), \tag{B.3}$$

$$s_m^{(1)} \equiv c_{Vv}\ln(T/T_0) - R_v\ln(\rho_m/\rho_{m0}^*) + \Lambda_0, \tag{B.4}$$

$$s_m^{(2)} \equiv C(T) + D(T)/\rho_m. \tag{B.5}$$

The specific entropy of condensate $C(T)$, the saturation vapor pressure $E(T)$, and its derivative $D(T) = dE(T)/dT$, along with the various constants in the formulas, have been defined in O90 for the synthetic condensate that continuously represents both ice and liquid water.

The Second Law of Thermodynamics

Since the publication of O90, muted but persistent criticisms have been heard against the use of the entropy as one of prognostic variables in an atmospheric model. Our general response in section 2b is supplemented below with specific details.

In the standard notation of thermodynamics (e.g., Morse 1969), the second law is stated as

$$dS \geq đQ/T, \tag{B.6}$$

where dS is the change of entropy of a given system from one equilibrium state to another, and $đQ$ the heat added to the system from an external source. The crossed d signifies an imperfect differential, implying that the exchanged amount of heat is not a function of the two equilibrium states but varies depending on the specific path the system takes during the transitional process. If *and only if* the process is reversible, $đQ$ can be written as the perfect differential dQ, since it is the same for any reversible path that connects the two equilibrium states, and (B.6) takes the equality $dS = dQ/T$.

If the process is irreversible, the inequality (B.6) does not tell what dS should be, even if $đQ$ is known. On the other hand, the entropy is a state variable defined at any equilibrium state and can be determined by the first law,

$$dU = đQ - đW, \tag{B.7}$$

along with, if permissible, the ideal gas law and the perfect gas assumption.[B.1] Note that the mechanical work done by the system, $đW$, is also an imperfect differential in irreversible processes, and that (B.7) requires both $đQ$ and $đW$ to be determined for a specified path. Thus, the irreversible processes that often arise in meteorology are configured to take place in a thermally and mechanically isolated container of a fixed volume, so that

$$đQ = đW = 0, \tag{B.8}$$

and, consequently, $dU = 0$.

For example, the mixing of dry air and water vapor from the initial state of each gas occupying a separate space at the same temperature to the final state of a homogeneous mixture in the combined space, is treated as the free expansion of each gas into the space originally occupied by the other gas. The temperature of perfect gases does not change in free expansion, but

[B.1] The internal energy of a perfect gas is a function of the temperature only.

an increase of the total entropy results from the volume expansion of each gas. This entropy due to the mixing of two different gases is already included in the definitions (B.1)–(B.5). If the two gases are the same, similar reasoning results in Gibbs' paradox: the entropy of a gas in a container may be decreased or increased merely by inserting or removing a partition. Therefore, the mixing of the same gas in two different states is treated as a process of temperature equalization. In particular, if the two initial states are at the same pressure and differ only in temperature, the final temperature is the mass-weighted mean of original temperatures and the pressure does not change. The entropy increases from the fact that the arithmetic mean of two different temperatures is always greater than their geometric mean.

The thermal diffusion in atmospheric models is a parameterization of the temperature equalization process at finite rates. For the gravitationally stratified dry atmosphere, it is commonly expressed in terms of the potential temperature θ as

$$\partial_t \theta = K \partial_{xx} \theta, \tag{B.9}$$

where K is the eddy diffusivity; for simplicity, only one spatial dimension, x, is used and advective terms are omitted. If we accept (B.9) as part of the modeled physics, an exactly equivalent equation can be derived in terms of the specific entropy, $s_a = c_{Pa} \ln\theta$, as

$$\partial_t s_a = K\{\partial_{xx} s_a + (\partial_x s_a)^2 / c_{Pa}\}. \tag{B.10}$$

The squared term on the rhs shows not only the fact that the entropy increases, but also that the rate of increase is rather small, since c_{Pa} is greater than typical spatial variations of s_a by two or three orders of magnitude. In the case of a moist atmosphere, the primary question is how to parameterize the process of diffusion for the mixture of dry air and water substance in various phases. If the decision, for example, is to equalize the entropy temperature (Hauf and Höller 1987), the dry entropy in (B.10) is simply replaced by the moist entropy. Therefore, as long as the defined parameterization is physically consistent, it can be expressed in different but physically equivalent forms; the choice between entropy and potential temperature is akin to the choice between Cartesian and curvilinear coordinates for the same geometric space.

As stated in section 2b, it is prudent that the parameterization of irreversible processes obeys the second law. In fact, it is not difficult to satisfy the law as an inequality. More difficult is the quantitative question, how much should the entropy increase? The question is especially relevant to numerical models in which the major role of the diffusive terms is to control numerical problems near the small-scale limit of the model resolution. When the coefficient K is chosen to be large enough for this purpose, the damping by the second-order diffusion extends far into larger scales where the damping is no longer required for numerical reasons, implying that the entropy increase is excessive in both the thermodynamic and informational sense. In order to focus the damping more selectively on small scales, many models now employ diffusion written in terms of fourth-order derivatives, although diffusion being second order is crucial for upholding the second law. In fact, fourth-order diffusion violates *Clausius' principle*, an alternative statement of the second law, by creating temperatures colder than those originally present. This dilemma, seemingly a mere glitch in the principle, is not likely to deter pragmatic modelers from the use of the fourth- or higher-order diffusion. The model presented in this paper performs without diffusive damping (see appendix C), so that it can implement the physically required diffusion without the dilemma. The verifiable determination (or parameterization) of the eddy diffusivity is a problem by itself, but it goes beyond the question about thermodynamic principles.

There are other irreversible processes that can not be discussed under the idealized condition (B.8). We may agree, for example, that the eddy kinetic energy in the inertial range of scales should eventually turn into heat by molecular viscosity. The problem arises in the models whose resolvable scales are far greater than the viscous range in millimeters, concerning the fate of the kinetic energy dissipated out of the resolvable scales. One option is to convert the kinetic energy of unresolvable eddies into heat as the immediate input to the entropy or internal energy of the resolvable scales; and another option is to simply ignore the lost kinetic energy. Of the two options, the first is quantitatively likely to be an exaggeration, especially if the eddy viscosity is chosen for computational reasons, while the second is absurd in principle but may be closer to the quantitative truth in short-term predictions, even though it is possible to contrive a theory to demonstrate otherwise (e.g., Bister and Emanuel 1998). Another question that is often raised by critics concerns the Earth's contributions to the cosmic entropy increase. We see no problem in principle. If the question is not merely philosophical but quantitative, the answer requires good estimates of $đQ$ and $đW$ by all the irreversible and reversible processes, regardless of whether a model uses the entropy or the internal energy.

APPENDIX C

The Cold Blob Experiment

A ''Workshop on Numerical Methods for solving Nonlinear Flow Problems'' was held on 11–13 September 1990 at the National Center for Supercomputing in Urbana, Illinois. For the purpose of comparing the behavior of a variety of numerical methods, a density current problem in the otherwise homogeneous and isentropic two-dimensional dry atmosphere was chosen as the test problem of the workshop. The complete definition of the problem, including the prognostic equa-

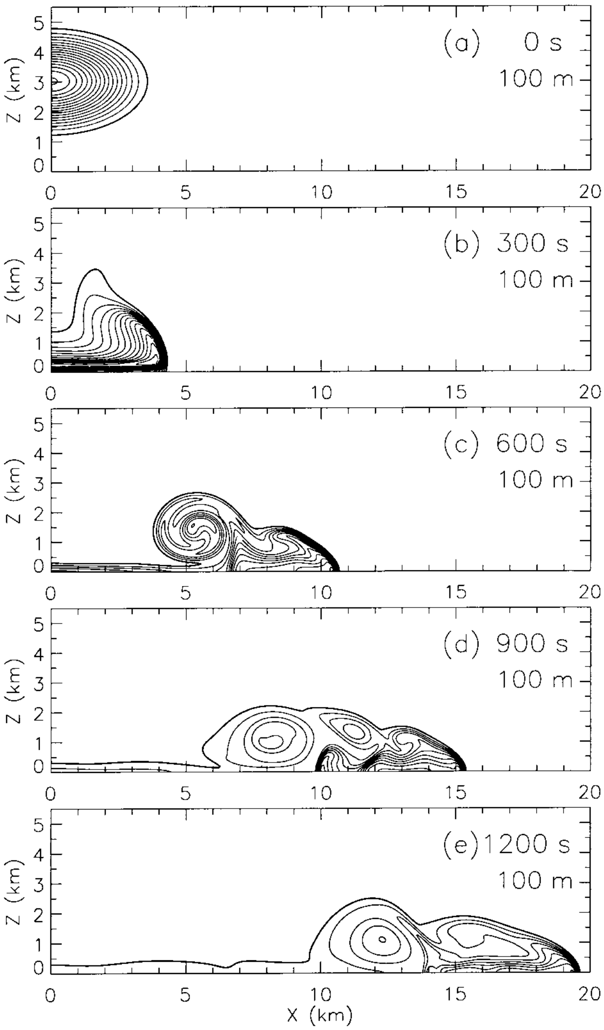

FIG. C1. (a)–(e) The solution of the test problem in the 100-m resolution run, shown by the contour plots of θ' at 300-s intervals. The thick contour line is for $\theta' = -0.5$ K (or $\theta = 299.5$ K), and other lines are drawn at 1-K intervals. The result is nearly identical with the 25-m resolution result obtained by the workshop "reference" model (Straka and Anderson 1993).

tions for mass continuity, horizontal and vertical momentum, and internal energy, may be found in Straka et al. (1991, hereafter SWWDA91) and also in Straka and Anderson (1993, hereafter SA93) with the quasi-compressible form of the equations. Our cubic spline-based spectral method, called the SAFER method (see section 5), was not ready at the time of the workshop, but was able to run the test a few months later. The result, shown below, confirms that our method is as competent as the best of the methods presented at the workshop.

The equations for this test are the same as described in section 4, with important exceptions: (i) all the moisture or precipitation related terms are deleted, and (ii) the diffusion terms are added as specified by the workshop. Thus, for the present discussions, $\rho = \rho_a$, $a = \ln(\rho/\rho_0)$, $s = s_a$, and K is the diffusion coefficient. Specifically, our prognostic equations are

$$\partial_t a + u\partial_x a + w\partial_z a + (\partial_x u + \partial_z w) = 0, \tag{C.1}$$

$$\partial_t u + u\partial_x u + w\partial_z u + \rho^{-1}\partial_x p = K(\partial_{xx} u + \partial_{zz} u), \tag{C.2}$$

$$\partial_t w + u\partial_x w + w\partial_z w + g + \rho^{-1}\partial_z p = K(\partial_{xx} w + \partial_{zz} w), \tag{C.3}$$

$$\partial_t s + u\partial_x s + w\partial_z s = K\{\partial_{xx} s + \partial_{zz} s + c_{Pa}^{-1}[(\partial_x s)^2 + (\partial_z s)^2]\}. \tag{C.4}$$

As discussed in appendix B, the squared gradient of entropy on the rhs of (C.4) makes this entropy equation an exact equivalent of the internal energy equation in the workshop definition, although these extra terms have hardly made any difference in numerical tests.

There is no need for the diagnostic procedures of section 2; the usual state variables, if necessary, are directly determinable from the predicted entropy s and log-density a:

$$\theta = \theta_0 \exp(s/c_{Pa}), \qquad p = p_0 \exp[(s + c_{Pa} a)/c_{Va}],$$
$$T = p/(\rho R_a), \tag{C.5}$$

where the subscript 0 denotes the constant reference values. The actual prediction, as discussed in sections 4b and 4c, is made in terms of the deviations (denoted with a prime) from the hydrostatically balanced background states (denoted with a circumflex). In particular, the pressure gradients in the momentum equations are given by

$$\rho^{-1}\partial_x p = \tau\partial_x a' + \partial_x \tau',$$
$$g + \rho^{-1}\partial_z p = \tau\partial_z a' + \tau'\partial_z \hat{a} + \partial_z \tau', \tag{C.6}$$

where the auxiliary diagnostic variable $\tau = p/\rho$ is related to the predicted a' and s' by

$$\tau = \hat{\tau} \exp[(s' + R_a a')/c_{Va}], \qquad \hat{\tau} = \hat{p}/\hat{\rho} = R_a \hat{T},$$
$$\tau' = \tau - \hat{\tau}. \tag{C.7}$$

Being reduced to the dry atmosphere, our equations are not substantially different from the traditional schemes with the prognostic pressure. In particular, the semi-implicit method in our fully compressible model and the quasi-compressible assumption on the pressure tendency equation are equally effective in handling unwanted acoustic waves.

The background states are defined to be isentropic at $\hat{\theta} = 300$ K with the surface pressure 1000 hPa. The horizontally symmetric domain of half-width 25.6 km and 6.4 km in height is specified. In order to start a density current, a cold elliptic blob of radii 4 km in x and 2 km in z, centered at $x = 0$ and $z = 3$ km, is prescribed as a temperature perturbation of -15 K at

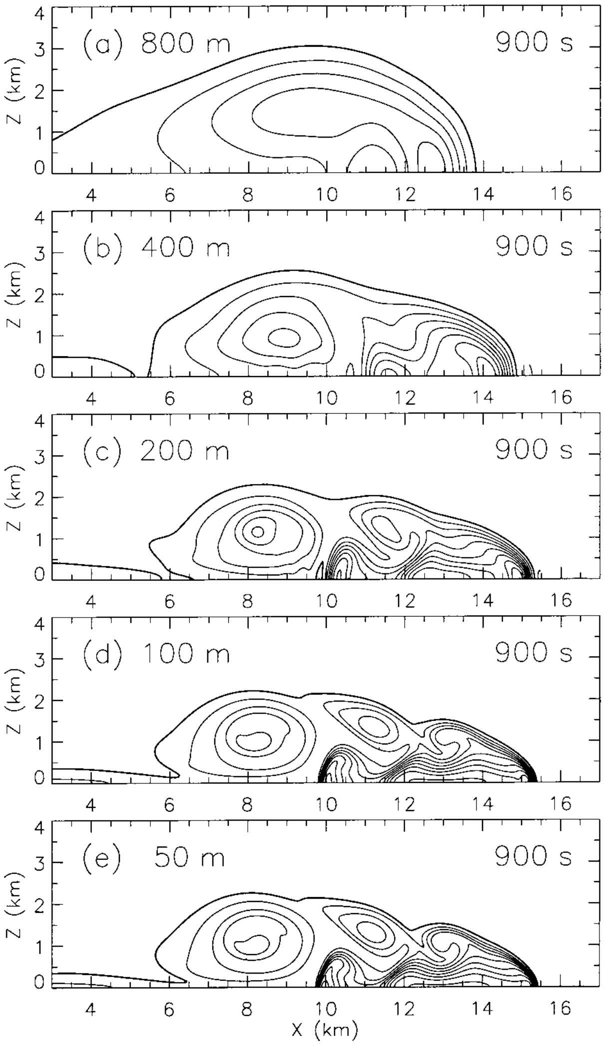

FIG. C2. The effects of model resolution: (a) 800, (b) 400, (c) 200, (d) 100, and (e) 50 m, shown at $t = 900$ s. The contours are for θ' as in Fig. 15. The fixed diffusion coefficient, $K = 75\ \mathrm{m^2\ s^{-1}}$, becomes more effective as the resolution is refined, so that the solutions converge from (a) to (e), and (d) and (e) are practically identical. In the coarser resolutions of (a) and (b), the built-in spectral filter is responsible for noise-free solutions within the respective range of resolvable scales.

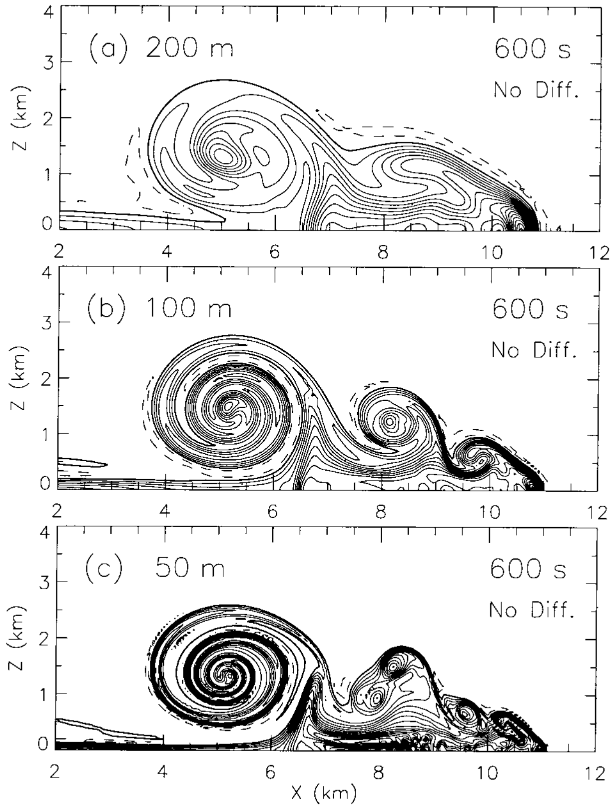

FIG. C3. The solutions of the same test problem but with no diffusion. The contour plots of θ' at $t = 600$ s are shown for the resolutions: (a) 200, (b) 100, and (c) 50 m. The contour intervals are 1 K as in earlier figures, although lines are now extremely crowded. The shear instability generates a greater number of rotary eddies as the resolution is refined, but no numerical difficulty is encountered in these runs. The fine structure of these eddies is also found in Skamarock and Klemp's (1993) adaptive-grid solutions with scaled-down diffusion.

the center. More precise definitions of the test problem, including the numerical values of physical constants, are found in SA93, and need not be repeated here, except for emphasizing that the diffusion coefficient K is fixed at 75 $\mathrm{m^2\ s^{-1}}$ for comparison purposes. The spatial resolution and the time step are optional; in our experiment, $\Delta x = \Delta z = 50$, 100, 200, 400, 800 m, and $\Delta t = 0.25$, 0.5, 1, 2, 4 s, respectively.

The result of the 100-m resolution run, depicting the initiation of a density current, generation of multiple rotors by Kelvin–Helmholtz instability and gradual dissipation, is shown in Fig. C1 by contour plots of θ' at 300 s intervals. This result may be compared with the 25-m resolution result by the workshop ''reference'' model in Fig. 1 of SWWDA91 and Fig. 3 of SA93. The agreement is nearly perfect. The contour intervals are 1 K in all these figures, but the absolute levels of contours are vague in the cited papers. In our Fig. C1; the thick contour line is for $\theta' = -0.5$ K (or $\theta = 299.5$ K), since this choice gives us the best agreement with the diagrams of the ''reference'' solution.

In the workshop, a particular emphasis was placed on the convergence of solutions. Fig. C2 answers this question by comparing the results of various resolutions at $t = 900$ s. The bottom two panels for 100 and 50 m are almost identical, and the middle for 200 m is still very similar; the loss of fine details is apparent at 400 m, and only the gross features of the advancing pool of cold air are captured at the 800-m resolution. When this figure is compared with Fig. 5 of SA93 and Fig. 3 of SWWDA91, two complimentary aspects of the present model stand out: (i) at finer resolutions, where the diffusion is dominant in the small-scale dynamics, the model accurately converges to the ultimate solution; (ii) at coarser resolutions, where the diffusion is ineffective, the model's spectral filter asserts control over the small-scale numerics and produces a reasonable solution within the resolvable scales. The workshop reference model apparently lacks (ii), so that its solution becomes fairly noisy at 200 m and much worse at 400 m. In application to a nested model, (ii) is an important property of our method, since the same set of physical equations may have to be solved in multiple domains of different resolution.

In order to gather further evidence that the model with no diffusion can handle highly nonlinear flows, we have run the test problem by setting $K = 0$ in (C.2)–(C.4). The results for the 200-, 100-, and 50-m resolutions at $t = 600$ s are shown in Fig. C3. It is obvious that the solutions do not converge. Instead, the shear instability generates a greater number of rotary eddies as the resolution is refined. No numerical difficulty is encountered in each run for 1200 s. We have no reference solution with which to compare, but Skamarock and Klemp (1993) show in their Figs. 4 and 5 the solutions of the adaptive-grid model with the finest local resolution of 28.7 m and scaled-down diffusion. The similarity in the fine structure of the eddies suggests the numerical veracity of our method.

REFERENCES

Asselin, R., 1972: Frequency filter for time integrations. *Mon. Wea. Rev.,* **100,** 487–490.

Betts, A. K., 1973: Non-precipitating cumulus convection and its parameterization. *Quart. J. Roy. Meteor. Soc.,* **99,** 178–196.

Bister, M., and K. A. Emanuel, 1998: Dissipative heating and hurricane intensity. *Meteor. Atmos. Phys.,* **65,** 233–240.

Burridge, D. M., 1975: A split semi-implicit reformulation of the Bushby–Timpson 10-level model. *Quart. J. Roy. Meteor. Soc.,* **101,** 777–792.

Chen, C., 1991: A nested grid, nonhydrostatic, elastic model using a terrain-following coordinate transformation: The radiative-nesting boundary conditions. *Mon. Wea. Rev.,* **119,** 2852–2869.

DeMaria, M., 1995: Evaluation of a hydrostatic, height-coordinate formulation of the primitive equations for atmospheric modeling. *Mon. Wea. Rev.,* **123,** 3576–3589.

——, S. D. Aberson, K. V. Ooyama, and S. J. Lord, 1992: A nested spectral model for hurricane track forecasting. *Mon. Wea. Rev.,* **120,** 1628–1643.

Droegemeier, K. K., and R. B. Wilhelmson, 1987: Numerical simulation of thunderstorm outflow dynamics. Part I: Outflow sensitivity experiments and turbulence dynamics. *J. Atmos. Sci.,* **44,** 1180–1210.

Eliassen, A., and E. Kleinschmidt Jr., 1957: *Dynamic Meteorology.* Vol. 47, *Handbuch der Physik: Geophysik II,* Springer-Verlag, 1045 pp.

Fovell, R. G., and Y. Ogura, 1989: Effect of vertical wind shear on numerically simulated multicell storm structure. *J. Atmos. Sci.,* **46,** 3144–3176.

——, and P.-H. Tan, 1998: The temporal behavior of numerically simulated multicell-type storms. Part II: The convective cell life cycle and cell regeneration. *Mon. Wea. Rev.,* **126,** 525–550.

Fulton, S. R., and W. H. Schubert, 1987: Chebyshev spectral methods for limited-area models. Part I: Model problem analysis. *Mon. Wea. Rev.,* **115,** 1940–1953.

Grabowski, W. W., and T. L. Clark, 1991: Cloud-environment interface instability: Rising thermal calculations in two spatial dimensions. *J. Atmos. Sci.,* **48,** 527–546.

Grell, G. A., J. Dudhia, and D. A. Stauffer, 1995: A description of the fifth-generation Penn State/NCAR mesoscale model (MM5). NCAR Tech. Note NCAR/TN-398+STR, 122 pp.

Hauf, T., and H. Höller, 1987: Entropy and potential temperature. *J. Atmos. Sci.,* **44,** 2887–2901.

Högström, U., 1988: Non-dimensional wind and temperature profiles in the atmospheric surface layer: A re-evaluation. *Bound.-Layer Meteor.,* **42,** 55–78.

Huschke, R. E., 1959: *Glossary of Meteorology.* Amer. Meteor. Soc., 638 pp.

Jordan, C. L., 1958: Mean soundings for the West Indies area. *J. Meteor.,* **15,** 91–97.

Kessler, E., 1969: *On the Distribution and Continuity of Water Substance in Atmospheric Circulation. Meteor. Monogr.,* No. 32, Amer. Meteor. Soc., 84 pp.

Kinzer, G. D., and R. Gunn, 1951: The evaporation, temperature and thermal relaxation-time of freely falling waterdrops. *J. Meteor.,* **8,** 71–83.

Klemp, J. B., and R. Wilhelmson, 1978: The simulation of three-dimensional convective storm dynamics. *J. Atmos. Sci.,* **35,** 1070–1096.

Kurihara, Y., and M. A. Bender, 1980: Use of a movable nested-grid model for tracking a small vortex. *Mon. Wea. Rev.,* **108,** 1792–1809.

Morse, P. M., 1969: *Thermal Physics.* 2d ed. W. A. Benjamin, 431 pp.

Ogura, Y., and N. A. Phillips, 1962: Scale analysis of deep and shallow convection in the atmosphere. *J. Atmos. Sci.,* **19,** 173–179.

——, and T. Takahashi, 1971: Numerical simulation of the life cycle of a thunderstorm cell. *Mon. Wea. Rev.,* **99,** 895–911.

Ooyama, K. V., 1982: Conceptual evolution of the theory and modeling of the tropical cyclones. *J. Meteor. Soc. Japan,* **60,** 369–380.

——, 1987: Scale-controlled objective analysis. *Mon. Wea. Rev.,* **115,** 2479–2506.

——, 1990: A thermodynamic foundation for modeling the moist atmosphere. *J. Atmos. Sci.,* **47,** 2580–2593.

Robert, A. J., 1969: The integration of a spectral model of the atmosphere by the implicit method. *Proc. WMO/IUGG Symp. on Numerical Weather Prediction,* Tokyo, Japan, Japan Meteorological Agency, VII-19–VII-24.

——, 1979: The semi-implicit method. *Numerical Methods used in Atmospheric Models,* GARP Publication Series, Vol. 2, GARP/WMO-ICSU Joint Organizing Committee, 439–437.

Rotunno, R., J. B. Klemp, and M. L. Weisman, 1988: A theory for strong, long-lived squall lines. *J. Atmos. Sci.,* **45,** 463–485.

Shchepetkin, A. F., and J. C. McWilliams, 1998: Quasi-monotone advection schemes based on explicit locally adaptive dissipation. *Mon. Wea. Rev.,* **126,** 1541–1580.

Skamarock, W. C., and J. B. Klemp, 1993: Adaptive grid refinement for two-dimensional and three-dimensional nonhydrostatic atmospheric flow. *Mon. Wea. Rev.,* **121,** 788–804.

Straka, J. M., and J. R. Anderson, 1993: Extension and application of a local, minimum aliasing method to multidimensional problems in limited-area domains. *Mon. Wea. Rev.,* **121,** 2903–2918.

——, R. B. Wilhelmson, L. J. Wicker, K. K. Drogemeier, and J. R. Anderson, 1991: Workshop on numerical methods for solving nonlinear problems. Preprints, *Ninth Conf. on Numerical Weather Prediction,* Denver, CO, Amer. Meteor. Soc., 274–278.

Tapp, M. C., and P. W. White, 1976: A non-hydrostatic mesoscale model. *Quart. J. Roy. Meteor. Soc.,* **102,** 277–295.

Tatsumi, Y., 1986: Spectral limited-area model with time-dependent lateral boundary conditions and its application to a multilevel primitive equation model. *J. Meteor. Soc. Japan,* **64,** 637–664.

Tremback, C. J., J. Powell, W. R. Cotton, and R. A. Pielke, 1987: The forward-intime upstream advection scheme: Extension to higher orders. *Mon. Wea. Rev.,* **115,** 540–555.

Tripoli, G. J., and W. R. Cotton, 1981: The use of ice-liquid water potential temperature as a thermodynamic variable in deep atmospheric models. *Mon. Wea. Rev.,* **109,** 1094–1102.

Weisman, M. L., W. C. Skamarock, and J. B. Klemp, 1997: The resolution dependence of explicitly modeled convective systems. *Mon. Wea. Rev.,* **125,** 527–548.

Yamasaki, M., 1977: A preliminary experiment of the tropical cyclone without parameterizing the effects of cumulus convection. *J. Meteor. Soc. Japan,* **55,** 11–31.

Zhang, D.-L., H.-R. Chang, N. L. Seaman, T. T. Warner, and J. M. Fritsch, 1986: A two-way interactive nesting procedure with variable terrain resolution. *Mon. Wea. Rev.,* **114,** 1330–1339.